Science Advances
AAAS

Supplementary Materials for

Broadband sensory networks with locally stored responsivities for neuromorphic machine vision

Guo-Xin Zhang *et al.*

Corresponding author: Xu-Dong Chen, chenxd@nankai.edu.cn; Tong-Bu Lu, lutongbu@tjut.edu.cn; Jin Zhang, jinzhang@pku.edu.cn

Sci. Adv. **9**, eadi5104 (2023)
DOI: 10.1126/sciadv.adi5104

This PDF file includes:

Supplementary Note 1. Synthesis of core-sheath SWNT@GDY nanotubes

1.1 Preparation of hexaethynylbenzene (HEB) monomer

Hexakis[(trimethylsilyl)ethynyl]benzene (HEB-TMS) was first synthesized according to the synthetic route presented in Supplementary Scheme 1 (*41*). Then 5 mg HEB-TMS monomers were dissolved into 75 mL CH_2Cl_2 solvent in a Schlenk reactor. 75 μL solution of tetrabutylammonium fluoride (1 M in tetrahydrofuran) was added into the HEB-TMS solution. After reaction at 0°C for 15 min under Ar atmosphere in the dark, HEB solution (in CH_2Cl_2) was obtained as the precursor for the subsequent coupling reaction.

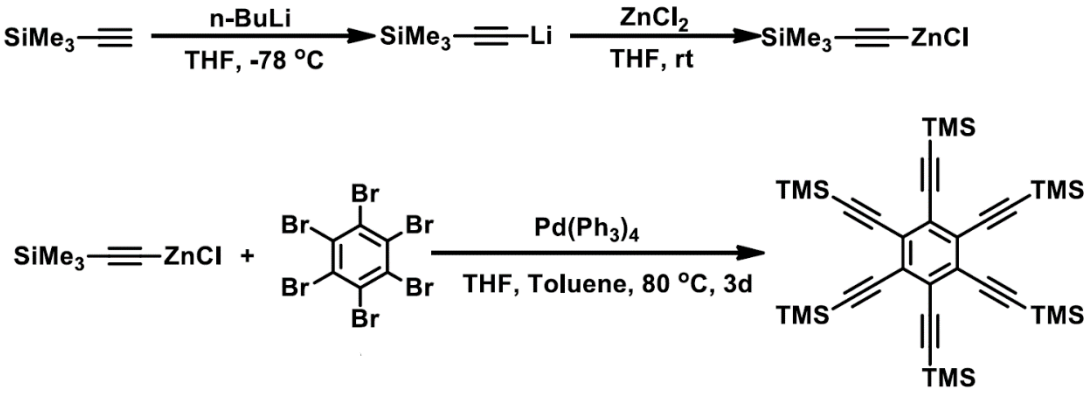

Scheme S1 Synthetic route for the HEB-TMS monomers.

1.2 Preparation of semiconducting SWNT toluene solution

Arc-discharged semiconducting single-walled carbon nanotubes (SWNTs, 20 mg) were first dissolved in 20 mL of toluene (*42*), followed by tip-sonicating for 30 min. The resultant suspensions were centrifuged with 40,0000 *g* for 1 h to remove the impurities. The upper 90% of the supernatants were collected for further use.

1.3 Synthesis of core-sheath SWNT@GDY nanotubes

A solution-phase epitaxial strategy was used to synthesize core-sheath SWNT@GDY nanotubes (*27-30*). 200 μL of as-prepared SWNT toluene solution was added to 5 mL of pyridine solution of copper acetate (2 mM) and 2 mL of toluene in a home-made reaction vessel. 5 mL of dichloromethane solution of HEB monomers (10 μM) was slowly added into the reaction vessel using an injection pump with a rate of 100 μL min^{-1}. After 24 h successive catalytic coupling reaction in Ar atmosphere and dark environment at room temperature, a GDY layer with thickness

of approximately 1 nm was synthesized wrapping the SWNT, forming a core-sheath SWNT@GDY structure as illustrated in Fig. 1c. Fig. S1 compares the Raman spectra of SWNT and SWNT@GDY. The radial breathing mode (RBM) and G band of SWNT is almost unchanged before and after the synthesis of GDY layer (*43*), indicating that the synthesis process does not damage the structure and change the property of SWNTs. In addition, the new Y' band at around 2195 cm^{-1} demonstrates the success synthesis of GDY (*30, 41*).

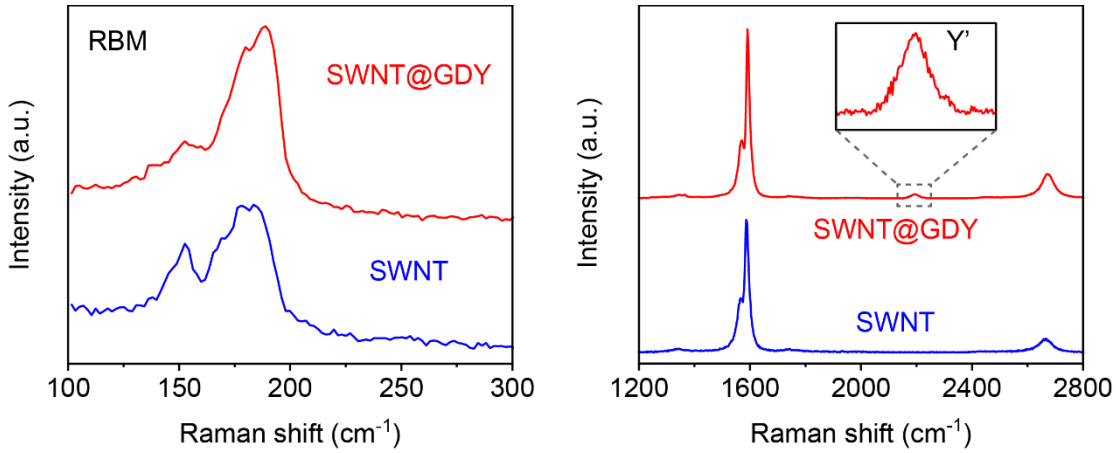

Fig. S1 Raman spectra of SWNT (blue) and SWNT@GDY (red), respectively. The inset in the right panel presents the zoomed-in Raman Y' band corresponding to GDY. The RBM and G band of SWNT are almost unchanged before and after GDY synthesis, indicating that the synthesis of GDY would not damage the structure and change the property of SWNT.

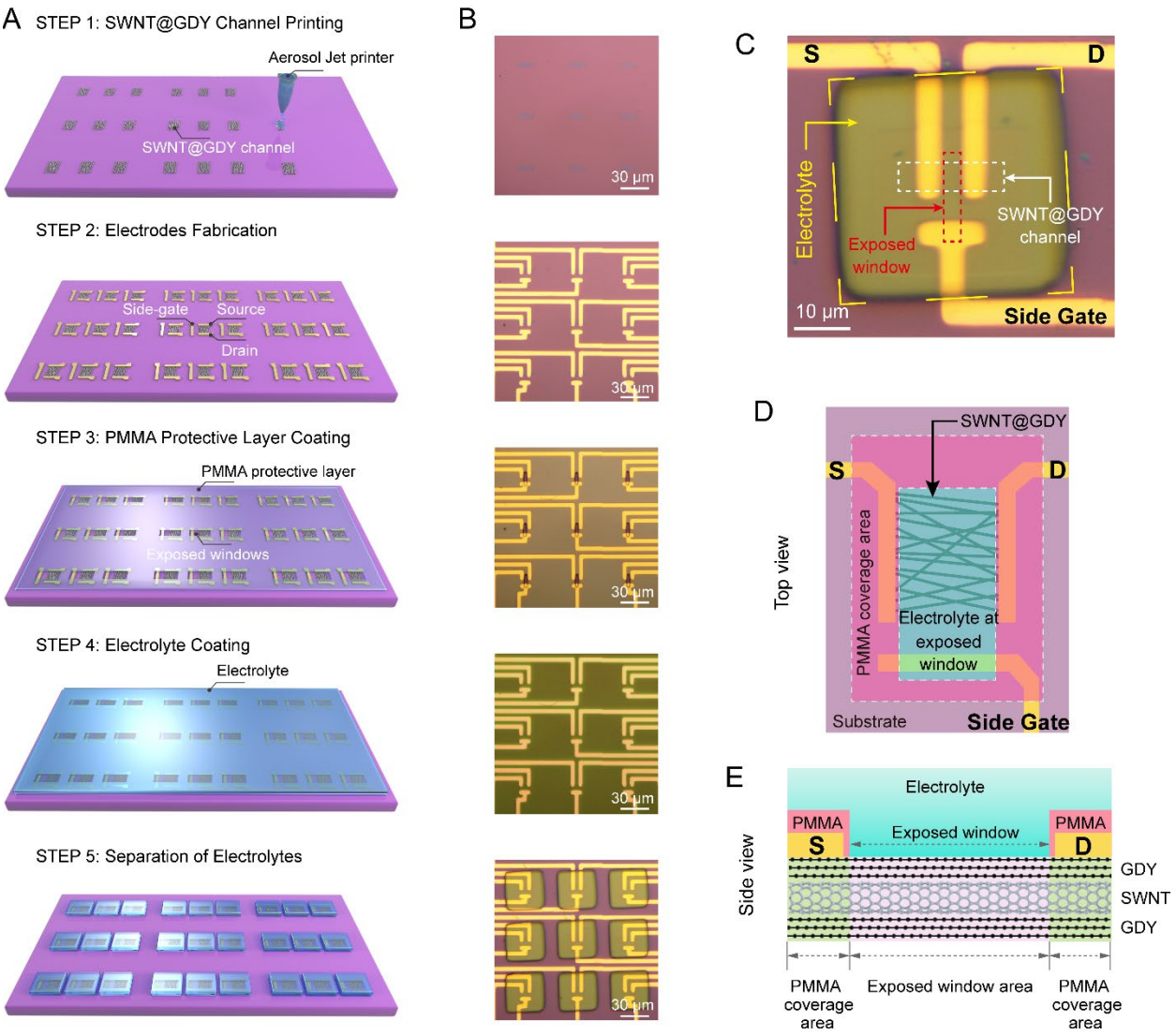

Fig. S2 Fabrication process and structure of the SWNT@GDY-based vision sensor array. **(A,B)** Illustration and corresponding optical images of the fabrication process of the sensor array. Step 1: SWNT@GDY channels with a thickness of approximately 10 nm are directly printed on the SiO_2/Si substrate by an Aerosol Jet printer. Step 2: the source, drain and side-gate electrodes (Cr/Au 10/50 nm) of the device array are fabricated by photolithography, thermal evaporation, and lift-off processes. Step 3, an insulated polymethyl methacrylate (PMMA) layer is spin-coated on the device surface to protect the source and drain electrodes from contact with the electrolyte, and specific windows on top of the SWNT@GDY channels and side gates were selectively exposed via electron-beam lithography (EBL). Step 4, the ion-gel electrolyte is spin-coated on top of the PMMA layer, connecting the exposed SWNT@GDY channel and side-gate. Step 5: The electrolytes of each device are separated by selective etching to avoid interference between

adjacent devices. **(C)** Optical image of an individual three-terminal device. **(D,E)** Schematic of the top-view and side-view of the device structure.

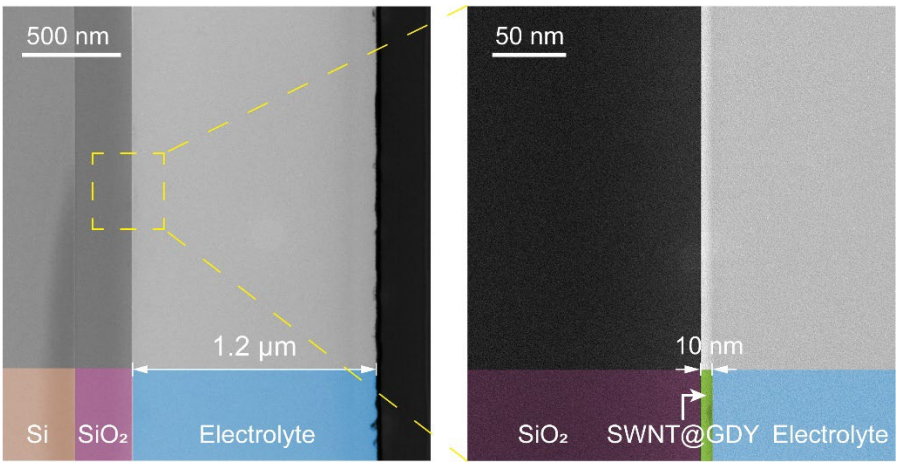

Fig. S3 TEM image of the cross-section of the device. The thickness of the SWNT@GDY channel and electrolyte are approximately 10 nm and 1.2 μm, respectively.

Supplementary Note 2. Mechanism for the non-volatile modulation of conductance and responsivity

2.1 Charge transport through the channel

Since SWNTs are p-type semiconductor, holes are the majority carriers in the channel. Fig. S4A illustrates the charge transport path between the source and drain electrodes. The SWNT@GDY has a core-sheath structure that SWNT is wrapped by GDY, and thus the electrodes have a direct contact with the outer GDY layer. As shown in fig. S5, the lateral conductance of GDY is almost 5 orders of magnitude lower than that of SWNT due to the numerous grain boundaries and defects in GDY, and thus the transport of charges in the lateral direction is mainly through the inner SWNT rather than GDY. On the other hand, the resistance of GDY film (approximately 1 nm) in the vertical direction is 10^6 ohms (including contact resistance between GDY and electrodes, fig. S6), which is 3 orders of magnitude smaller than that of SWNT channel. Thus holes from the drain electrode can inject into SWNT through the GDY layer and transport in SWNT in the lateral direction, and then pass through the GDY layer to reach the source electrode (fig. S4A). In addition, as illustrated in fig. S4B, the source and drain electrodes are protected by a PMMA layer from contact with the electrolyte, and only the SWNY@GDY channel under the exposed window area can contact the electrolyte. The intercalation of Li^+ ions into GDY and thus the modulation of conductance and photoresponse of the device mainly occur in this area. The resistance of the residual parts (PMMA coverage area) can be considered as constant. Thus the channel can be divided into three parts: two constant resistances (including contact resistance, resistance of GDY layer in vertical direction, and resistance of SWNT in the coverage area) and one electrolyte-gated phototransistor (SWNT@GDY channel under the exposed window) are connected in series (fig. S4C). The resistance of the device is dominated by the center phototransistor.

2.2 Non-volatile modulation of the conductance and responsivity

As shown in fig. S4D, a positive V_G pulse (0.5 V) can drive Li^+ ions in electrolyte penetrate into GDY layer, and the static electric field induced by the Li^+ ions leads to the decrease of the hole concentration (and thus the conductance) in the p-type SWNT channel under the exposed window area. After removing the V_G pulse, the intercalated Li^+ ions can still be restricted in GDY due to the diffusion barrier of Li^+ ions in GDY (fig. S4E), and thus resulting in a non-volatile modulation of the conductance. The extraction of Li^+ ions from GDY layer back to bulk electrolyte is realized

by applying an opposite (–0.5 V) V_G pulse. After removing the intercalated Li^+ ions in GDY layer, the device returns to its initial state.

As for the responsivity, the photoresponse mainly occurs at the area under the exposed window since the residual SWNT@GDY is covered by the electrodes. The numerous alkyne bonds in GDY are active as positive-charge-attracting magnets (*36, 37*) and the intercalated Li^+ ions in GDY can attract electrons. Photogenerated holes or electrons will be attracted to the charge-trapping sites in GDY and these trapped charges induce the change of the channel conductance (photocurrent) via photogating effect. While the hole-attracting alkyne bonds dominate the photoresponse, the trapped holes will induce a negative photoresponse, and in turn, the electron-attracting Li^+ ions will induce a positive photoresponse. By controlling the concentration of intercalated Li^+ ions in GDY, the responsivity can be modulated in both negative and positive regimes.

2.3 Crucial role of the GDY layer for the non-volatile modulation

The intercalation and storage of Li^+ ions in the GDY layer play a crucial role for the non-volatile modulation of the conductance and responsivity. Previous works have demonstrated that the accumulation of ions at the interface of the channel and electrolyte would induce the volatile change of the conductance (*44-47*), since the accumulated ions would gradually diffuse back to the bulk electrolyte after the gate pulse driven by the concentration gradient. In contrast, the intercalated ions in the channel would induce a non-volatile change of the conductance via electrochemical doping or redox (*35, 39, 44, 45, 48, 49*). For the device based on core-sheath SWNT@GDY, a V_G pulse of 0.5 V, 1 s could induce a non-volatile change of the channel conductance from 4 nS to 0.4 nS (fig. S7A). As a comparison, a device based on bare SWNTs with the same structure was fabricated, which exhibited a volatile response to a 0.5 V, 1 s V_G pulse (fig. S7B). In general, the ions can penetrate into the channel from the electrolyte when the gate voltage exceeds a certain range (*45, 50*). As shown in fig. S7B, the SWNT-based device realized a non-volatile change of the channel conductance while V_G exceeded 4 V. These results indicate that the intercalation of Li^+ ions into the GDY layer is realizable for a 0.5 V gate bias due to the evenly distributed pores (*51, 52*), while the penetration of Li^+ ions into the SWNT requires a much large (4 V) gate voltage. In addition, the photoresponse of the SWNT-based device cannot be modulated even after applying various V_G pulses (±0.7 V, 20 ms, fig. S8), indicating the important role of GDY for the non-volatile modulation of responsivity.

To further demonstrate the intercalation of Li^+ ions into the GDY layer, rather than the SWNT, electron energy loss spectroscopy (EELS) and Raman spectroscopy were performed. Fig. S9 presents the EELS mapping of Li for the cross-sectional SWNG@GDY and SWNT channels after applying a V_G pulse. After removing the electrolyte, a strong Li signal was still observed in the SWNT@GDY channel (V_G = 0.5 V), which indicated that Li^+ ions intercalated into the SWNT@GDY. For the bare SWNT channel, Li signal was hardly observed for the case of V_G = 0.5 V, and an obvious Li signal presented while V_G = 5 V. In addition, the Raman spectra of the SWNT channel after applying V_G pulses with different amplitudes were shown in fig. S10. The Raman spectra were almost unchanged while V_G was smaller than 3.5 V, and a significantly enhanced Raman D band was observed while V_G exceeding 3.5 V, since the injection of Li^+ ions would damage the structure of SWNTs and induce defects. The EELS mapping and Raman spectra are consistent with the volatile/non-volatile change of the channel conductance (fig. S7). All these results demonstrate that GDY plays a crucial role for the intercalation of Li^+ ions and non-volatile modulation of conductance and responsivity, with a small V_G pulse (e.g., 0.5 V).

2.4 Influence of the GDY layer thickness

The thickness of the shell GDY layer used in this work was approximately 1 nm, which was almost the thinnest GDY film that has been reported. Fig. S11 presents the absorption spectra of SWNT and GDY film with a thickness of 1 nm. The absorption of 1 nm thick GDY is much smaller than that of SWNT@GDY, which indicates that light is mainly absorbed by the core SWNT. With the increase of the GDY thickness, more light would be absorbed by the shell GDY layer, which would lead to the decrease of photoresponse and disrupt the linear relationship between the photocurrent and light intensity. In addition, a thicker GDY layer would degrade the electrical performance of the device. Fig. S4A illustrates the charge transport path between the source and drain electrodes. Holes from the drain electrode inject into SWNT through the GDY layer and transport in SWNT in the lateral direction, and then pass through the GDY layer to reach the source electrode. As shown in fig. S6, the resistance of a 1 nm thick GDY film in vertical direction was 10^6 ohms (including the contact resistances between electrodes and GDY), which is much smaller than that of SWNT channel. However, with the increase of the GDY thickness, the conductance of the GDY film in vertical direction degrades seriously, which would restrict the charge transport between the electrodes and SWNT channel. Thus a thin GDY film with 1 nm thickness is suitable for our device.

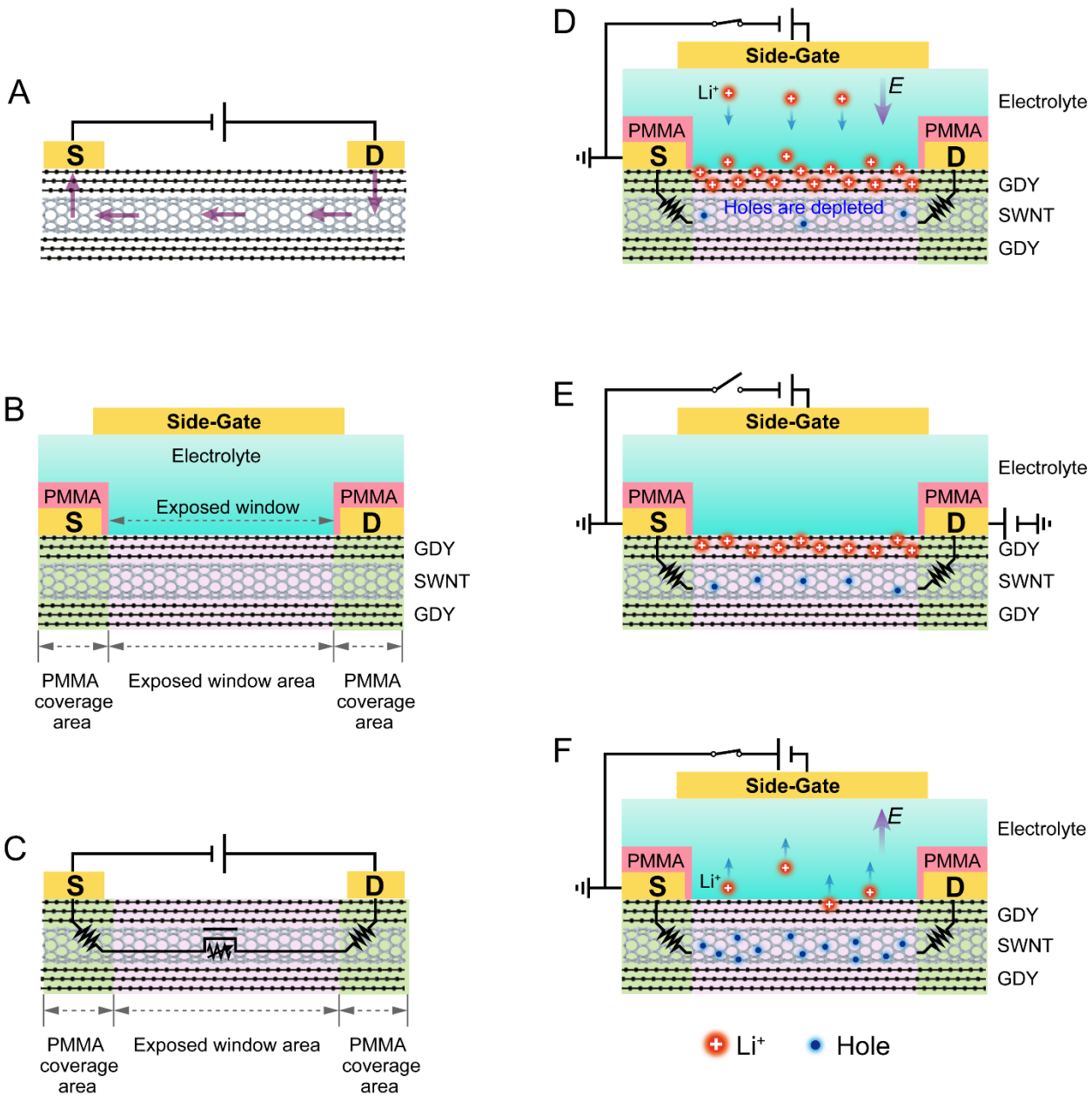

Fig. S4 Mechanism for the non-volatile modulation of channel conductance. (**A**) The charge transport path between the source and drain electrodes. Holes from the drain electrode inject into SWNT through the GDY layer and transport in SWNT in the lateral direction, and then pass through the GDY layer to reach the source electrode. (**B**) Schematic of the structure of the SWNT@GDY-based device. The source and drain electrodes are protected by a PMMA layer from contact with the electrolyte. A specific window is exposed by EBL on top of the channel, and only the SWNT@GDY under the exposed window area can contact the electrolyte, and the residual area are covered by PMMA. Noteworthily, for a clear view, the side-gate of the device is drawn

on top of the electrolyte in fig. S4. In fact, the side-gate is coplanar with the source and drain electrodes. (**C**) The equivalent circuit of device channel. The channel can be divided into three parts: PMMA coverage areas around the source and drain electrodes with constant resistances (including the contact resistance between electrode and GDY layer, the resistance of GDY layer in vertical direction, and the resistance of SWNT in the coverage area) and exposed area under the specific window with a Li^+-ion modulated conductance. Since the resistances at the PMMA coverage areas are much smaller than that of the exposed window area, the conductance and photoresponse of the device are dominated by the center phototransistor. (**D**) Driven by a positive gate voltage (V_G), positively charged Li^+ ions in electrolyte migrate from the bulk to the electrolyte/GDY interfaces, and due to the evenly distributed large pores of GDY, Li^+ ions can penetrate into GDY layer with a small gate bias. Noteworthily, a much higher gate bias is required for the penetration of Li^+ ions into SWNT (*53*), and thus we can control the penetration of Li^+ ions into the GDY layer while keeping the SWNT channel impermeable to Li^+ ions by applying a small V_G (0.5 V). The intercalated Li^+ ions in GDY layer can be regarded as positive charges captured in GDY, and an electric-double-layer (EDL) with high capacitance is formed locally nearby the SWNT, significantly changing the carrier density and thus the conductance of the SWNT via the EDL gating effect. (**E**) After removing the V_G pulse, the diffusion barrier of Li^+ ions in GDY restricts the diffusion of Li^+ ions captured in GDY layer back to the electrolyte without an external electric field. As a result, the intercalated Li^+ ions would retain in GDY layer even after removing external gate bias, resulting in a non-volatile modulation of the conductance and responsivity of the device. That is, the weights, i.e., conductance and responsivity, are locally stored. (**F**) The extraction of Li^+ ions from GDY layer back to bulk electrolyte is realized by applying an opposite (negative) V_G pulse. After removing the intercalated Li^+ ions in GDY layer, the device returns to its initial state.

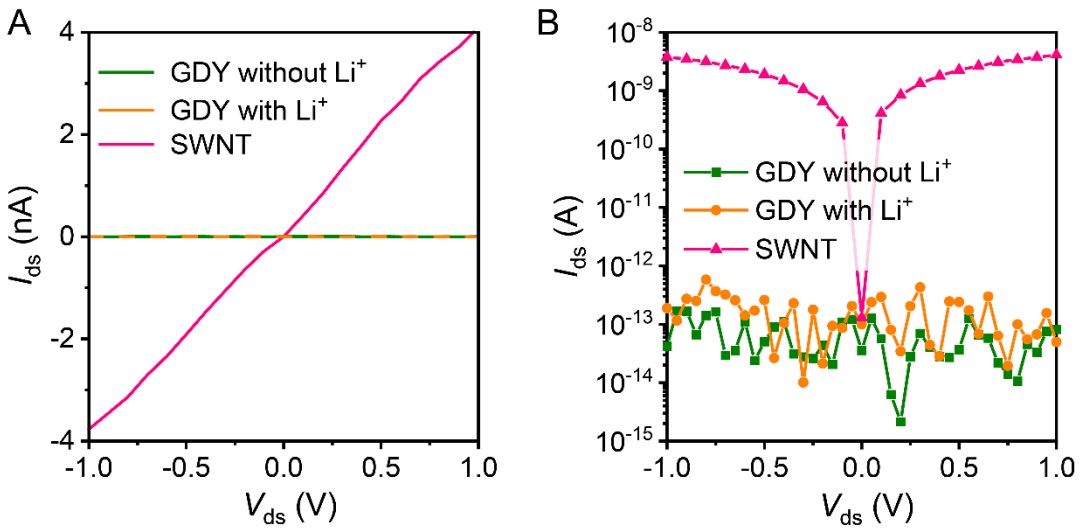

Fig. S5 *I*–*V* curves of lateral GDY and SWNT with V_{ds} sweeping from –1 V to 1 V in linear (**A**) and logarithmic (**B**) coordinates. The GDY used in this work is almost dielectric with/without the intercalation of Li^+ ions, demonstrating that the transports of charges between the source and drain is mainly through the SWNT channel.

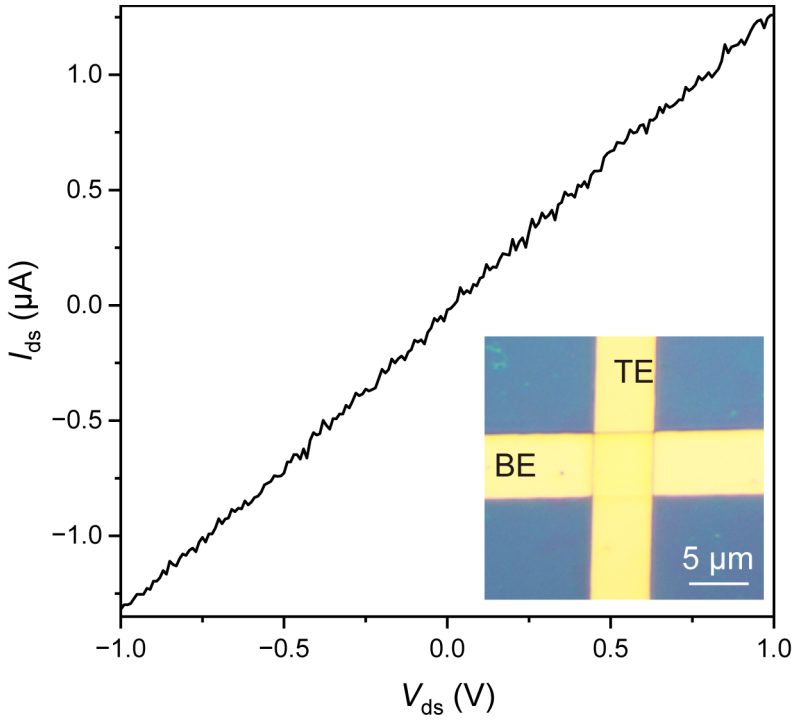

Fig. S6 *I–V* curve of the vertical Au/GDY/Au structure. The thickness of the GDY film was 1 nm. The inset is the optical image of the vertical Au/GDY/Au structure, in which TE and BE represent the top electrode and bottom electrode, respectively, and the GDY is sandwiched between the TE and BE.

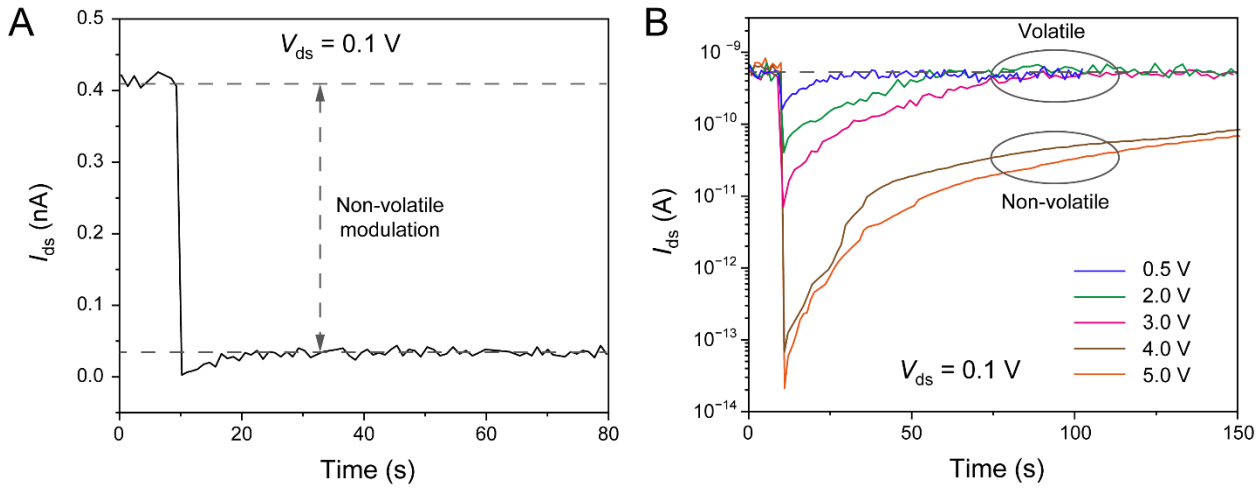

Fig. S7 Response of devices based on SWNT@GDY and SWNT triggered by V_G pulses with different amplitudes. (**A**) For the SWNT@GDY-based device, a 0.5 V, 1 s V_G pulse could induce a non-volatile change of the conductance, indicating the intercalation of Li^+ ions. (**B**) For the SWNT-based device, the conductance presented a volatile change when V_G pulses with amplitudes of 0.5 V, 2 V, and 3 V were applied, while the non-volatile change was realized by applying V_G pulses with larger amplitude (4 V and 5 V). The volatile change of conductance is induced by the accumulated Li^+ ions at the SWNT/electrolyte interface via the EDL gating effect, while the non-volatile change of the conductance is ascribed to the intercalation of Li^+ ions into the SWNT (*44, 45, 50*).

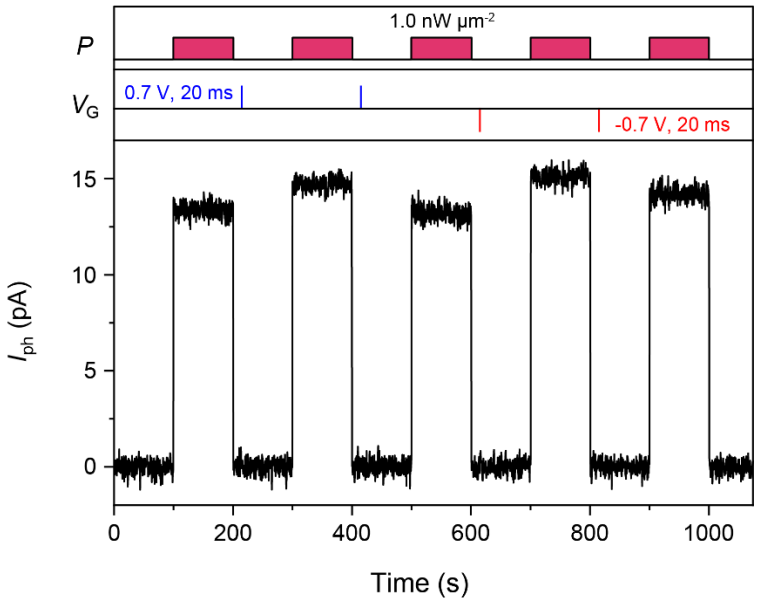

Fig. S8 Photoresponse of the SWNT-based electrolyte-gated phototransistor. Positive and negative V_G pulses were first applied, and the photocurrents were measured after the dark currents of the device becoming stable. The photocurrents were almost unchanged even after positive and negative V_G pulses, indicating that the responsivity of the device cannot be non-volatile modulated.

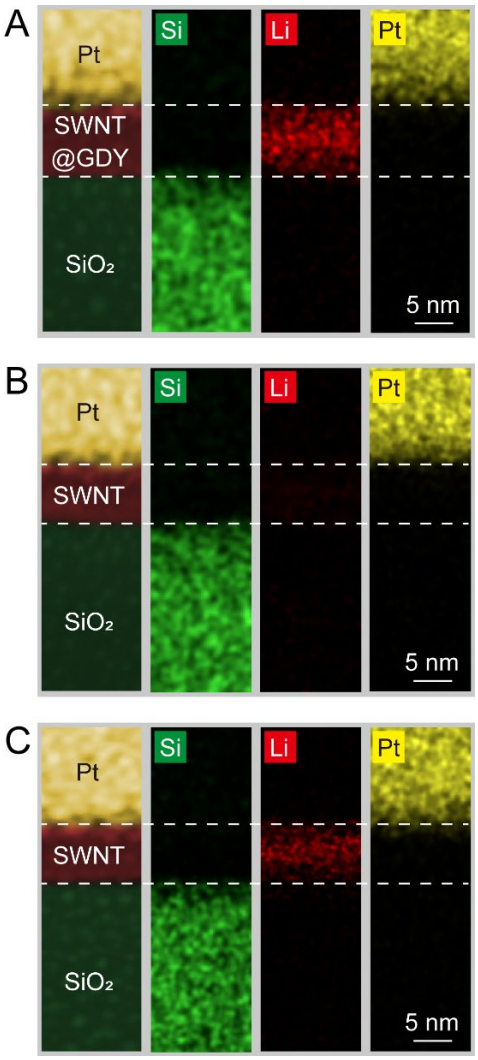

Fig. S9 EELS mapping images of the cross-sectional SWNT@GDY and SWNT channels after applying V_G pulses. (**A**) SWNT@GDY channel after applying a 0.5 V V_G pulse. (**B**) SWNT channel after applying a 0.5 V V_G pulse. (**C**) SWNT channel after applying a 5.0 V V_G pulse. The left panels in (**A–C**) are the high-angle annular dark field (HAADF) images of the cross-sectional SWNT@GDY and SWNT channels, and the left three panels correspond to the EELS mapping images of Si, Li and Pt, respectively. The samples were prepared as following: one SWNT@GDY-based device and two SWNT-based devices were fabricated, followed by applying a 0.5 V, 1 s V_G pulse to the SWNT@GDY-based device and one SWNT-based device, while the other SWNT-based device was applied to a 5.0 V, 1 s V_G pulse. Then the electrolytes of these three devices were dissolved to remove the Li^+ ions in bulk electrolytes and expose the SWNT@GDY and SWNT channels. Finally the cross-sectional TEM samples were prepared by focused ion beam (FIB). The Pt above the SWNT@GDY and GDY layers was introduced during the FIB process.

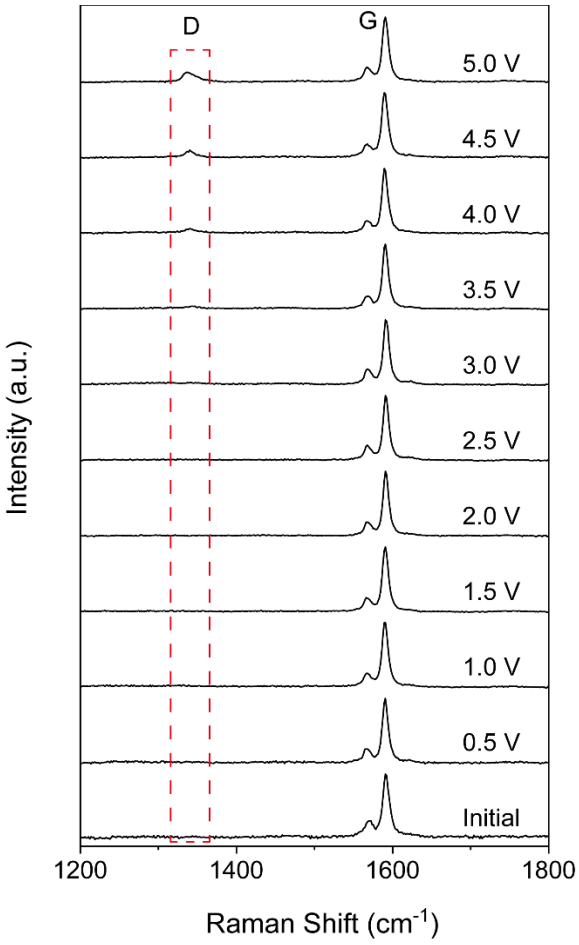

Fig. S10 Raman spectra of the SWNT channel after applying V_G pulses with amplitudes of 0.5–5 V. A significant Raman D band appeared at ~1340 cm^{-1} while the V_G pulse exceeding 3.5 V, indicating the appearance of defects in SWNTs.

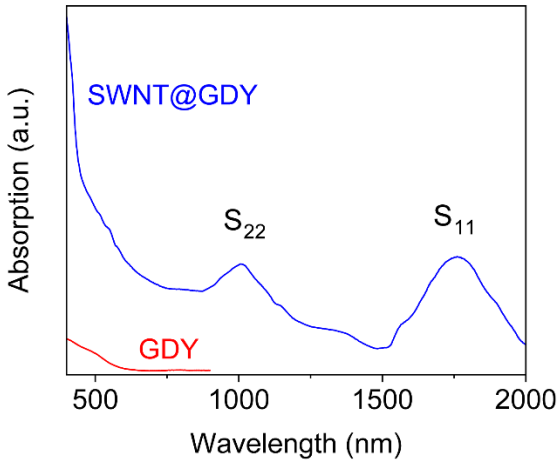

Fig. S11 Absorption spectrum of core-sheath SWNT@GDY and GDY. The core-sheath SWNT@GDY has a broadband absorption in range of 400–2000 nm, and the absorption peaks at around 1750 nm and 1000 nm correspond to the S_{11} and S_{22} peaks of semiconducting SWNTs, respectively (*54*). The absorption spectrum of GDY corresponds to the absorption of a 1 nm thick GDY film, which is much smaller than that of SWNT@GDY, indicating that the light is mainly absorbed by the inner SWNT.

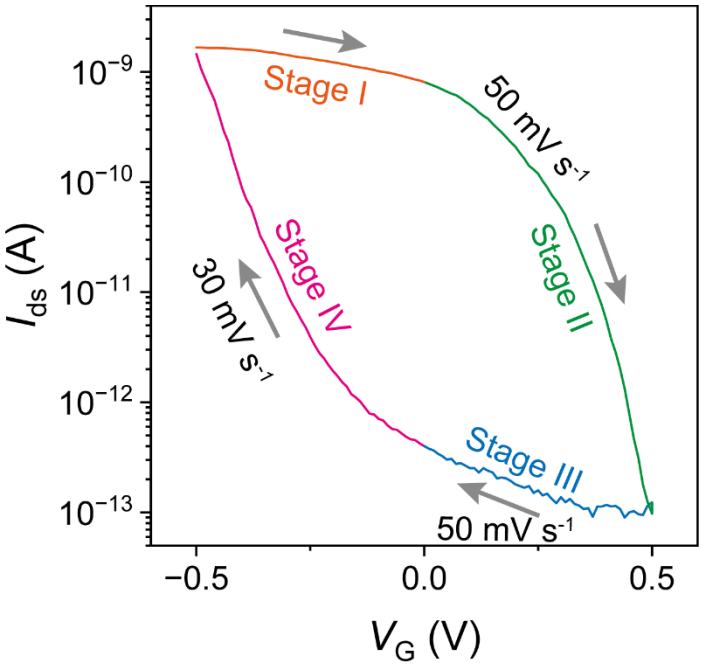

Fig. S12 Transfer curve of the device with different sweeping rates. The entire sweeping process of V_G can be divided into four stages: Stage I, –0.5 V to 0 V, ClO_4^- ions accumulate at the GDY/electrolyte interface, but they cannot intercalate into the GDY layer due to its large size. Stage II, 0 V to 0.5 V, Li^+ ions begin to accumulate at the GDY/electrolyte interface and intercalate into the GDY layer. Stage III, 0.5 V to 0 V, more Li^+ ions intercalate into the GDY layer. Stage IV, 0 V to -0.5 V, parts of intercalated Li^+ ions in the GDY layer are extracted by the negative gate bias. That is, in the sweeping process, the time for the intercalation of Li^+ ions is longer than that for the extraction of Li^+ ions. If the sweeping rate is constant for the entire process, some Li^+ ions still remain in the GDY layer after the sweeping process due to the asymmetrical time for the intercalation and extraction of Li^+ ions, and thus the conductance is decreased after sweeping (Fig. 2A in the main text). In order to extract all the intercalated Li^+ ions during the sweeping process, a longer extraction time for stage IV is required (a slower sweeping rate). In this case, the conductance can return to its origin.

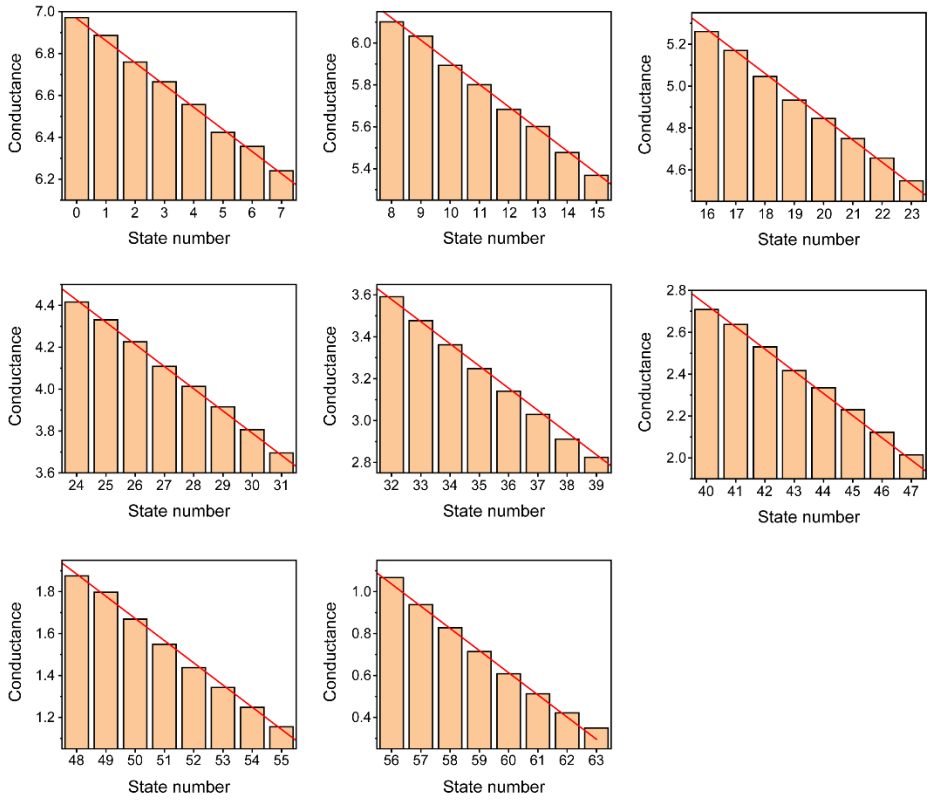

Fig. S13 64 conductance states achieved by applying V_G pulses. This is an enlargement of Fig. 2B in the main text, and the red line is the linearly fitted line of the 64 conductance states. State 0 represents the initial conductance of the device before applying V_G pulses. While a 0.5 V, 1 ms V_G pulse is applied to the device, the intercalated Li^+ ions in GDY will induce a decrease of the conductance via EDL gating effect, and thus the conductance state is changed from approximately 7.0 nS (state-0) to 6.9 nS (state-1). This change is non-volatile, just as shown in fig. S14. While more V_G pulses are applied, the conductance will be further decreased. Finally, by applying 63 V_G pulses, the conductance of the device can be linearly modulated from approximately 7.0 nS to 0.3 nS, forming 64 (including state-0) discrete states.

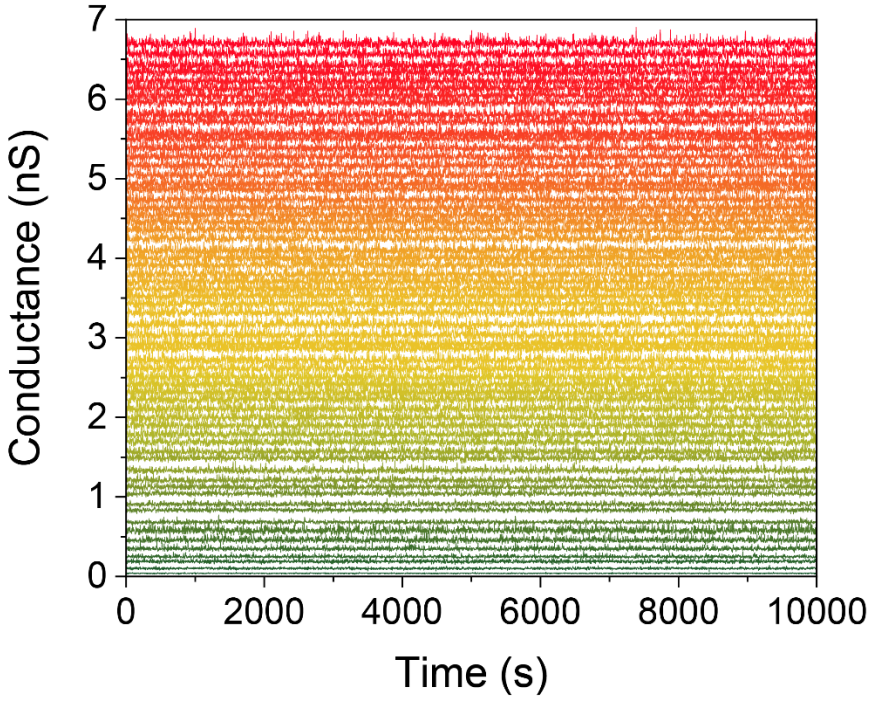

Fig. S14 Retention characteristics of the device at 64 conductance levels. Corresponding to Fig. 2B in the main text, by applying different numbers of V_G pulses, the device can be programmed to 64 discrete conductance levels, and the retention characteristics were measured by applying a 0.1 V read voltage for 10^4 s.

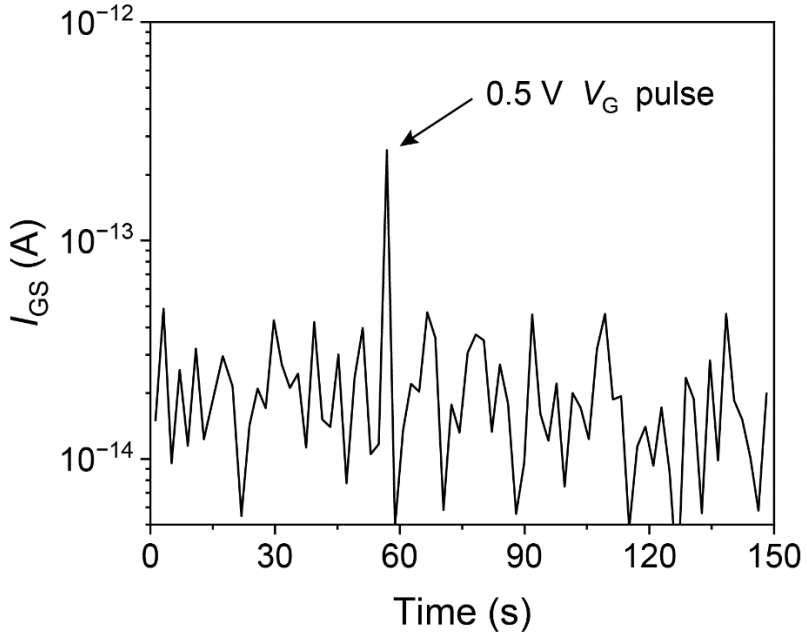

Fig. S15 The leakage current (I_{GS}) of the device measured by applying a 0.5 V V_G pulse.

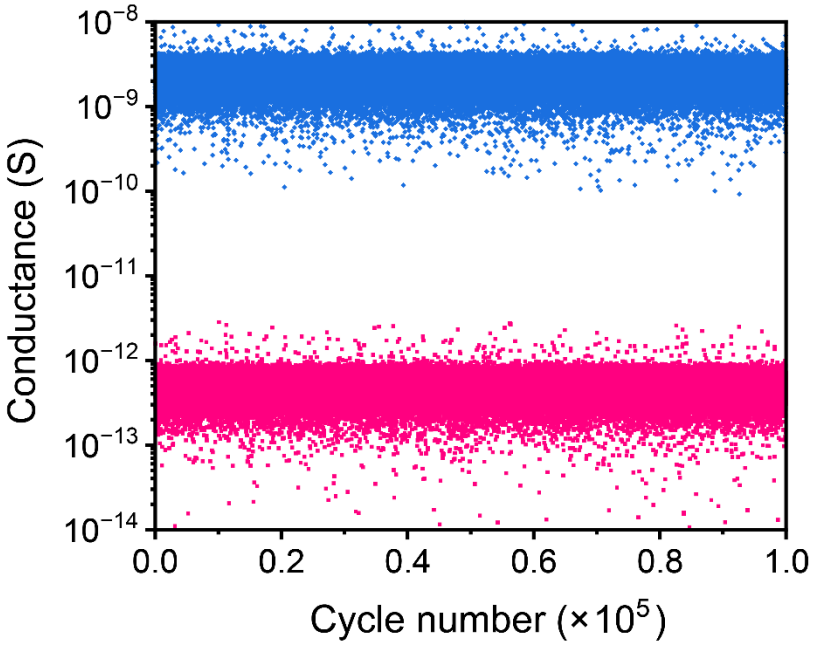

Fig. S16 Cyclic endurance of the device measured by alternatively applying ±0.5 V, 1 s V_G pulses. The device was switched between the high-conductance and low-conductance states for 10^5 times, and no obvious degradation was observed during whole test.

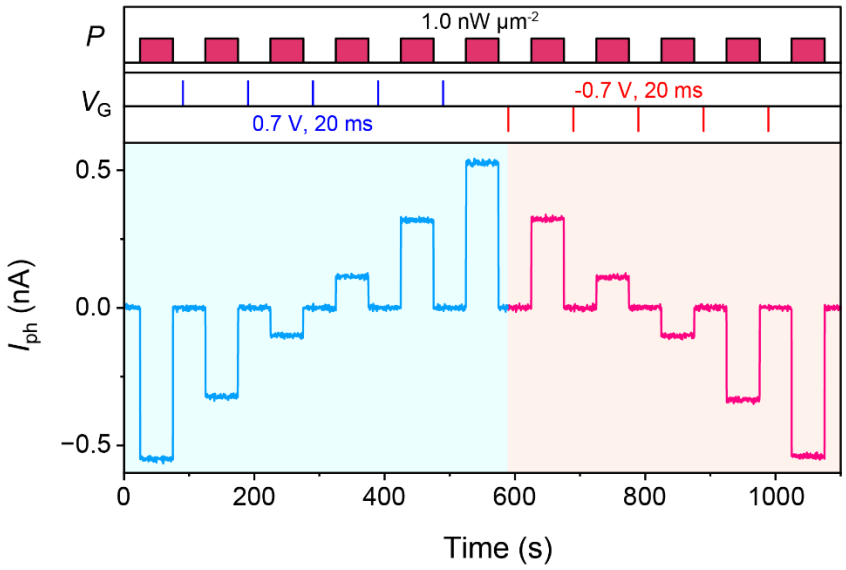

Fig. S17 Photocurrents of the device measured with different responsivities. Five positive (0.7 V, 20 ms) and five negative (–0.7 V, 20 ms) V_G pulses were sequentially applied to change the responsivity of the device, and after each V_G pulse the photocurrent was measured by irradiating a 532 nm light with intensity of 1.0 nW μm^{-2}. By applying positive V_G pulses, the photocurrent gradually evolves from negative to positive, and in turn, it gradually returns to initial negative value by applying negative V_G pulses, indicating the reversible modulation of responsivity in both positive and negative regimes. **Noteworthily, the photoresponse was measured with a latency of 30 s after each V_G pulse, and the changed photocurrents from negative to positive and back to negative undoubtedly demonstrated the non-volatile modulation of responsivity.**

Supplementary Note 3. Linear, symmetrical and identical conductance and responsivity updates in sensory networks

For the implementation of in-memory and in-sensor computing, linear, symmetrical and identical weight updates with small device-to-device and cycle-to-cycle variations (DDV&CCV) are essential. Here a closed-loop programming method (*25*) was used to circumvent the nonlinear and asymmetric weight update issue and minimize the DDV and CCV. In order to minimize the number of V_G pulses required for the weight update, the linear modulation regime of all the 27 devices was first determined.

As shown in fig. S18, the initial responsivity of the device is first measured, and this value is defined as $-R_0$ (the initial responsivity is negative). Then a series of +0.5 V, 1 ms V_G pulses (basic V_G pulses for closed-loop programming) are applied to the device, and the corresponding responsivities after each V_G pulse are measured. While the responsivity value close to $+R_0$ (the opposite value of the initial responsivity), stop to apply positive V_G pulses, and in turn, a series of negative V_G pulses (–0.5 V, 1 ms) are applied to the device until the responsivity returns to $-R_0$. Thus we obtain a complete responsivity update curve consisting of potentiation and depression. Then a boundary value R is defined, and the responsivities in range of $\pm R$ (centered around zero) are linearly fitted, obtaining a fitting parameter of R-squared. The responsivity is considered as linear update while the fitted R-squared > 0.99, and the linear modulation regime is defined as the largest R with R-squared > 0.99. Noteworthily, the responsivities in the potentiation and depression curves are fitted separately, and both the two fitted R-squared parameters should be larger than 0.99. All the linear modulation regimes of the 27 devices were measured using this approach (fig. S19A). The intersection of all the 27 linear regimes is defined as the final linear modulation regime, since it can ensure that all the device can be linearly modulated in this regime. Here the linear modulation regime for responsivity is approximately in ±10 mA W^{-1}. The linear modulation region of the conductance for all the 27 devices is defined using similar processes, which is in range of 0.4–7.0 nS (fig. S19B). The conductance and responsivity in the linear modulation regimes are equally divided into 32 levels, acting as the weights (5-bit precision) for the neural networks.

As described in the Materials and Methods section in the main text, after each epoch, the updated weights (responsivity and conductance) are calculated by backpropagating the gradients of the loss function. And the updated weights should be programmed to the device array hardware. Here we used the closed-loop programming method (fig. S20) to update the weights of the device array one

device by one device. Using responsivity as an example, the initial responsivity of the first device is measured by applying a 1.0 nW cm^{-2} illumination with a read voltage of 0.1 V. Compared to the target responsivity, if the measured responsivity is smaller (larger) than the target one, a +0.5 V, 1 ms (–0.5 V, 1 ms) V_G pulse is applied to the first device to increase (decrease) the responsivity. After that, the responsivity is measured and compared to the target one again. This process is repeated until the measured responsivity is within the margin of the target responsivity. Thus the responsivity update for the first device is completed, and the following devices are programmed in sequence using the same method, until all the 27 devices in the array are programmed to the target values. After that, we will check all the responsivity again to ensure all the weights are correctly updated. A similar process is performed to program the conductance of the device array to the updated value, one device by one device. In the conductance update process, a positive V_G pulse (0.5 V, 1 ms) is applied to decrease the conductance; and in turn, a negative V_G pulse (–0.5 V, 1 ms) is applied to increase the conductance.

Fig. S21, S22 present the 32 conductance and responsivity states achieved by the 27 devices using this closed-loop programming method, demonstrating that all the target conductance and responsivity levels can be programmed precisely. The 27 devices were further programmed to these 32 states for 1000 times, and fig. S23, S24 shows the statistics of the 1000 repetitions. These results demonstrate that the closed-loop programming method can update the conductance and responsivity linearly, symmetrically and identically.

On the average, it takes two V_G pulses to program the conductance to the adjacent level, and for the case of responsivity, three V_G pulses are required to update the responsivity to the adjacent one. Given the energy consumption for an individual V_G pulse is approximately 50 aJ ($E = V_G \times I_{GS} \times t_{duration}$), the average energy consumption for the update of conductance and responsivity between the adjacent levels are approximately 0.1 fJ and 0.15 fJ, respectively.

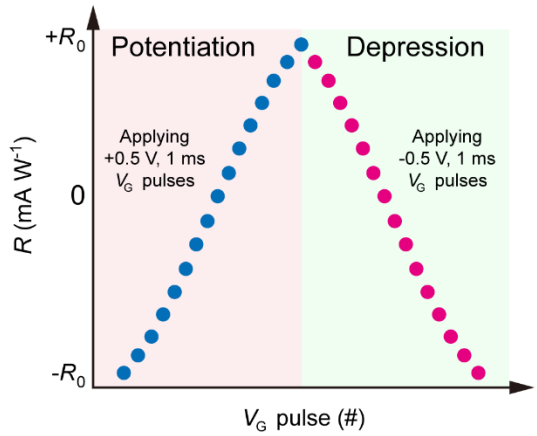

Step 1: apply a series of positive and negative V pulses, and measure the corresponding responsivity after each V_G pulse.

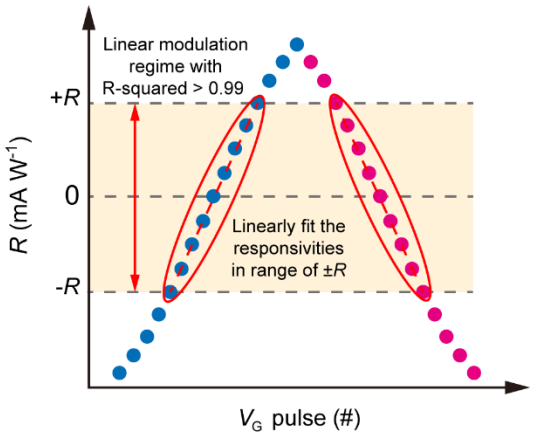

Step 2: linearly fit the responsivities in range of ±R, and define the linear regime with R-squared > 0.99.

Fig. S18 Defining the linear modulation regime for responsivity update. Step 1, update the responsivity by applying a series of +0.5 V, 1 ms V_G pulses (potentiation) and –0.5 V, 1 ms V_G pulses (depression), obtaining a complete responsivity update curve in range of ±R_0 (–R_0 is the initial negative responsivity before applying V_G pulses, and +R_0 is the largest value during responsivity update). Step 2, define a boundary value of R, and linearly fit the responsivities in range of ±R. While the fitted parameter of R-squared > 0.99, the responsivities in range of ±R are considered as linear update, and the linear modulation regime is defined as the largest R with R-squared > 0.99.

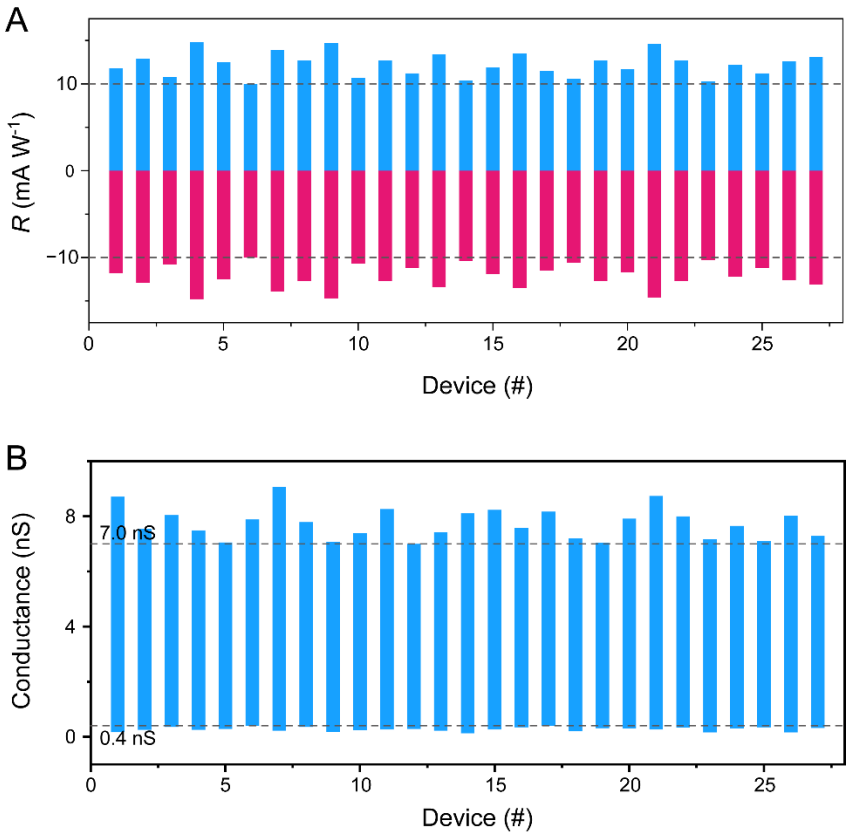

Fig. S19 Linear modulation regimes of the responsivity (**A**) and conductance (**B**) for all the 27 devices. The final linear modulation regime is the intersection of all the 27 linear regimes, so that all the devices can update linearly in this regime.

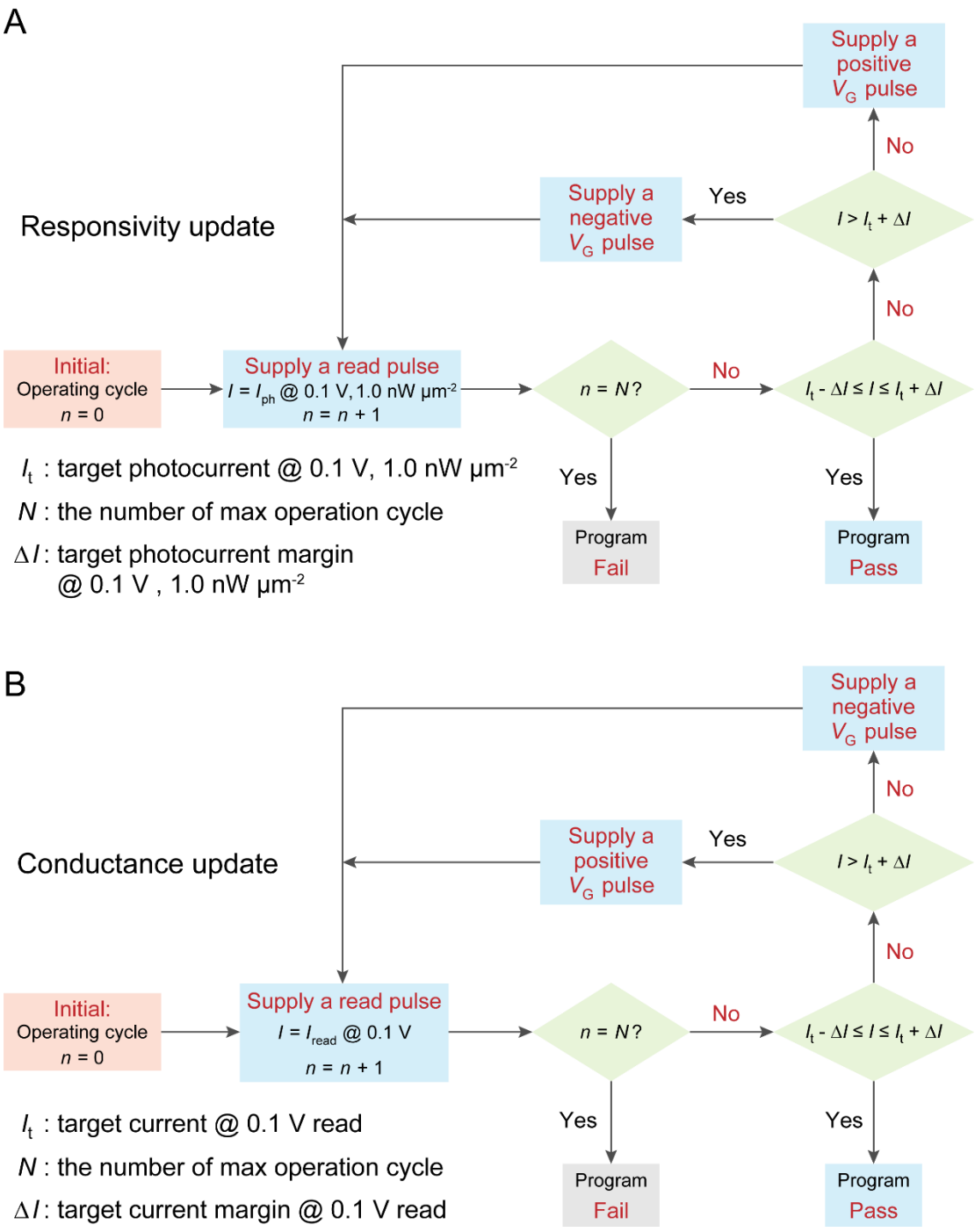

Fig. S20 Flowcharts of the closed-loop programming operations for responsivity update (**A**) and conductance update (**B**), respectively. For responsivity update, a positive (+0.5 V, 1 ms) and a negative (–0.5 V, 1 ms) V_G pulse were used to increase and decrease the conductance, while the increase and decrease of conductance were realized by applying a negative (–0.5 V, 1 ms) and a positive (+0.5 V, 1 ms) V_G pulse, respectively.

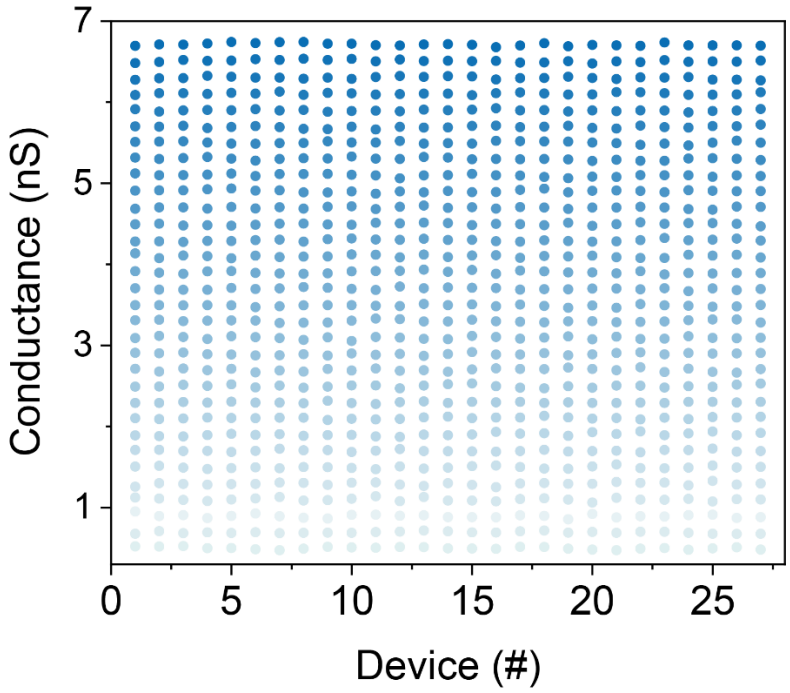

Fig. S21 32 conductance states achieved by the 27 devices using the closed-loop programming method.

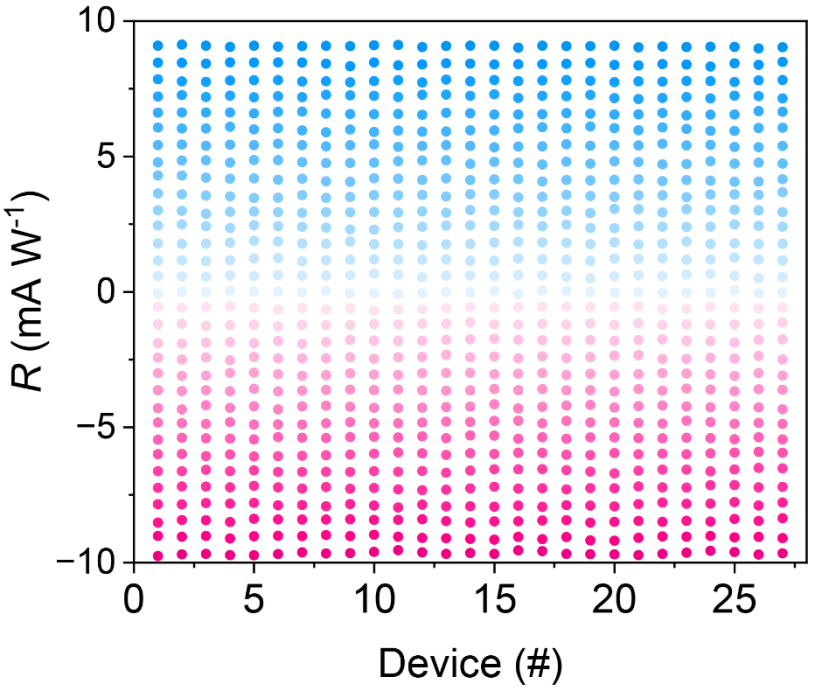

Fig. S22 32 responsivity states achieved by the 27 devices using the closed-loop programming method.

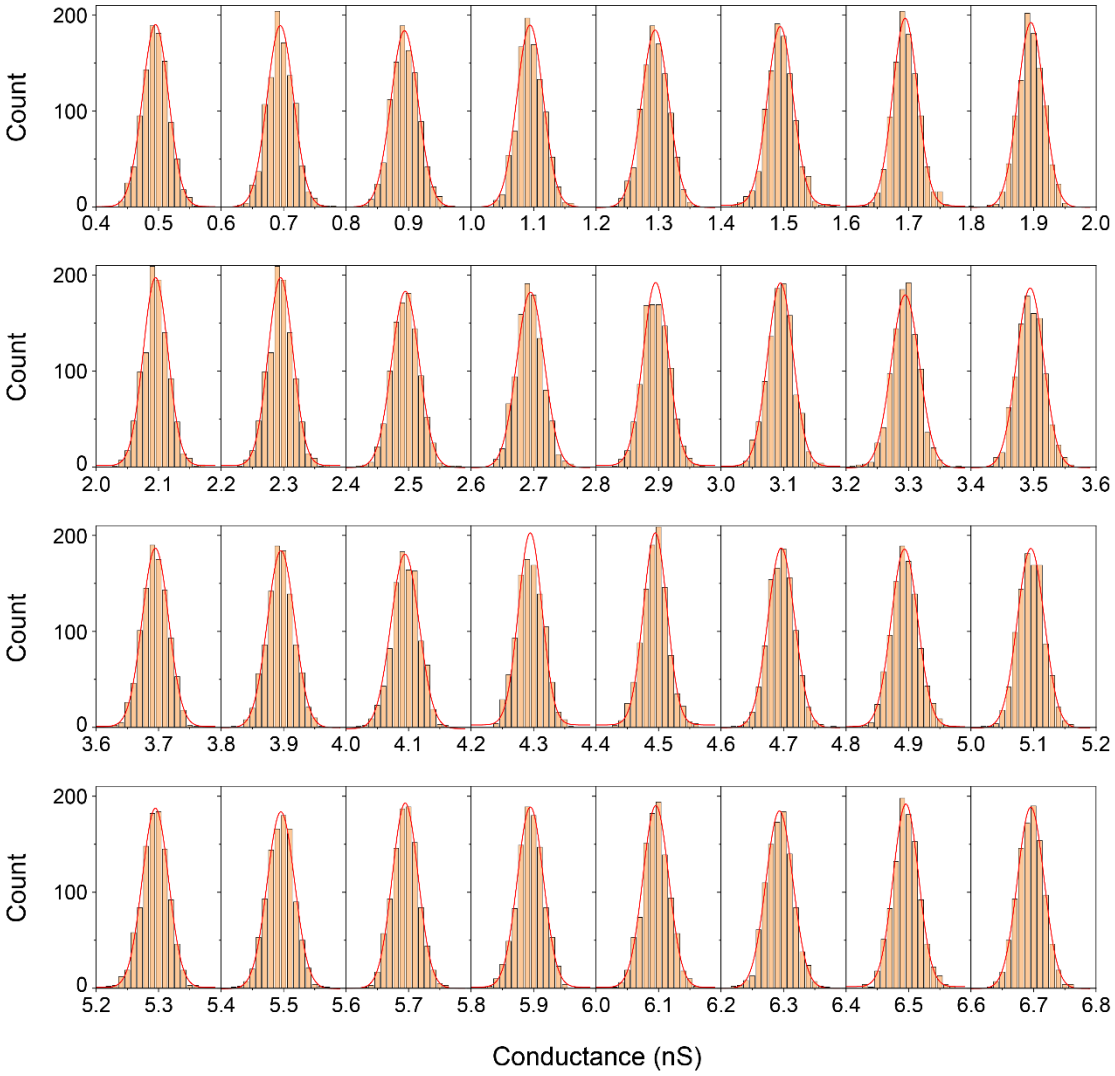

Fig. S23 Statistics of the 32 conductance states achieved by the 27 devices for 1000 repetitions.

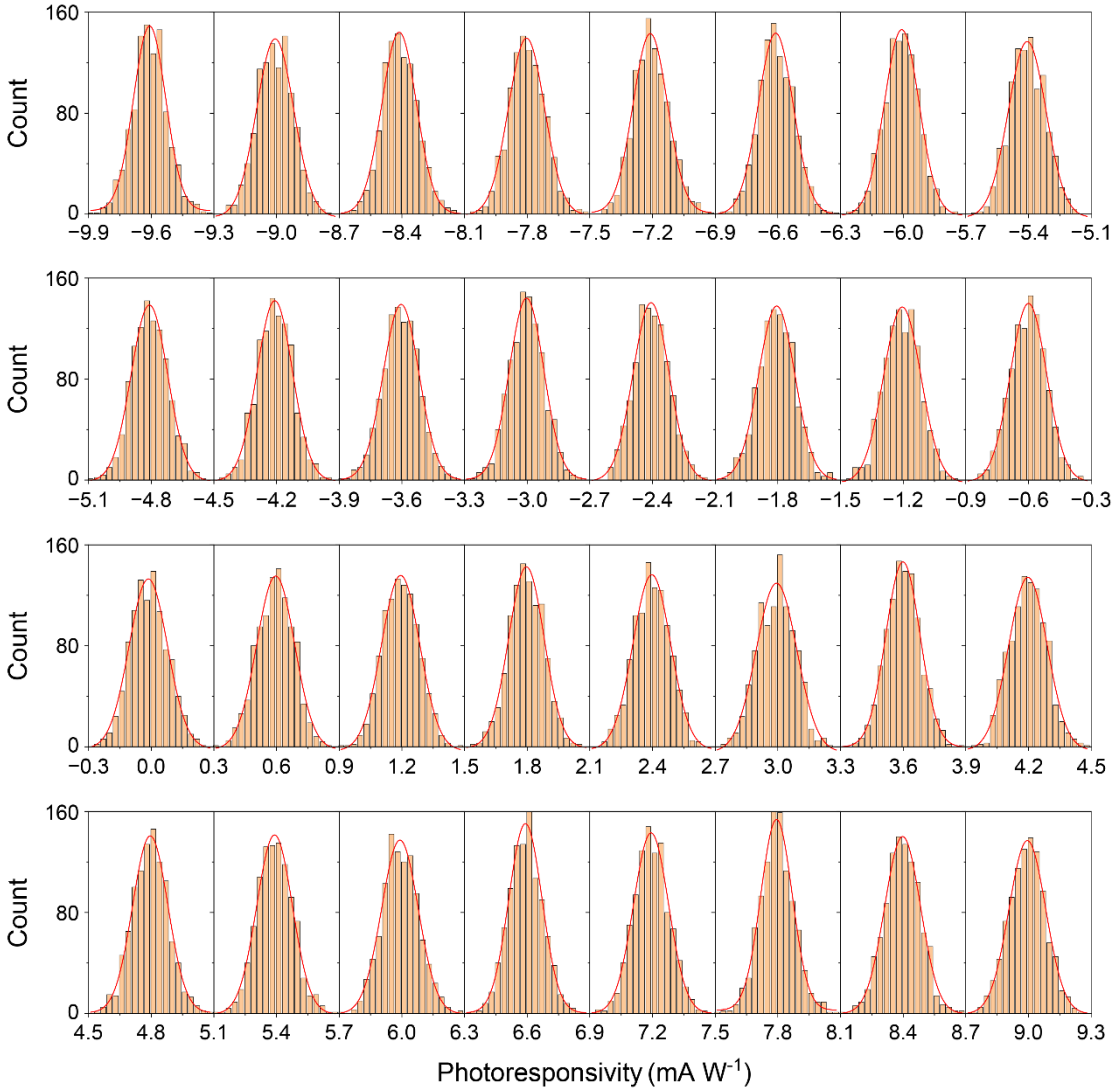

Fig. S24 Statistics of the 32 responsivity states achieved by the 27 devices for 1000 repetitions.

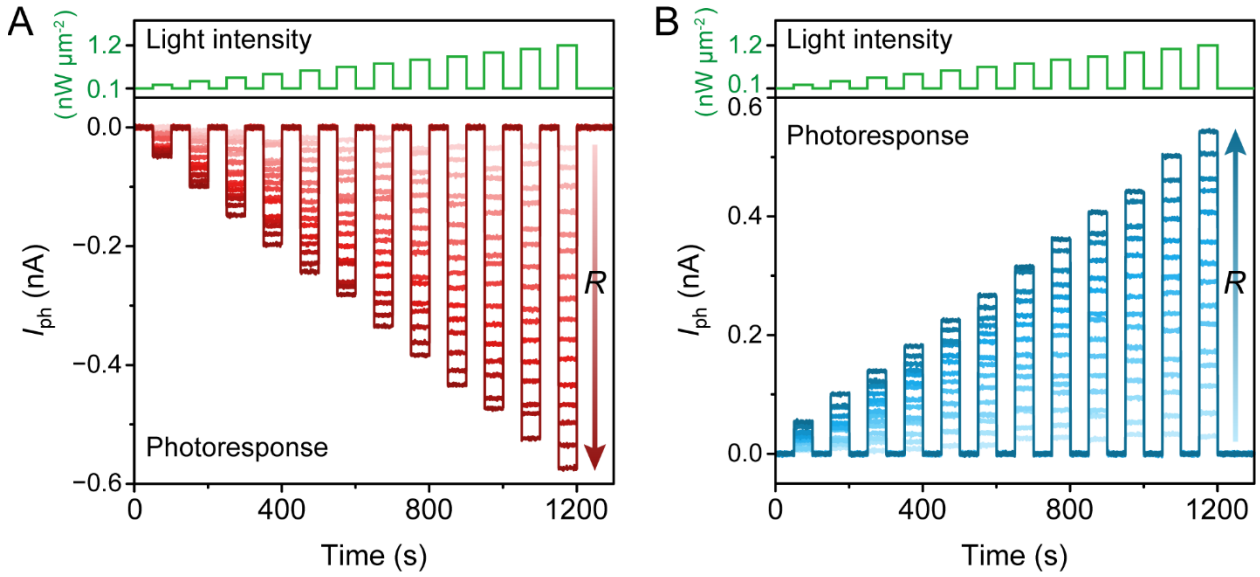

Fig. S25 Light-intensity dependent photoresponse of the device with different responsivities. Optical pulses with intensity in range of 0.1–1.2 nW μm^{-2} with a step of 0.1 nW μm^{-2} were applied to the device. The gradually deepening red and blue curves in (**A**) and (**B**) represent the photoresponse of the device with gradually increased amplitude of responsivity in negative (**A**) and positive (**B**) regimes, respectively.

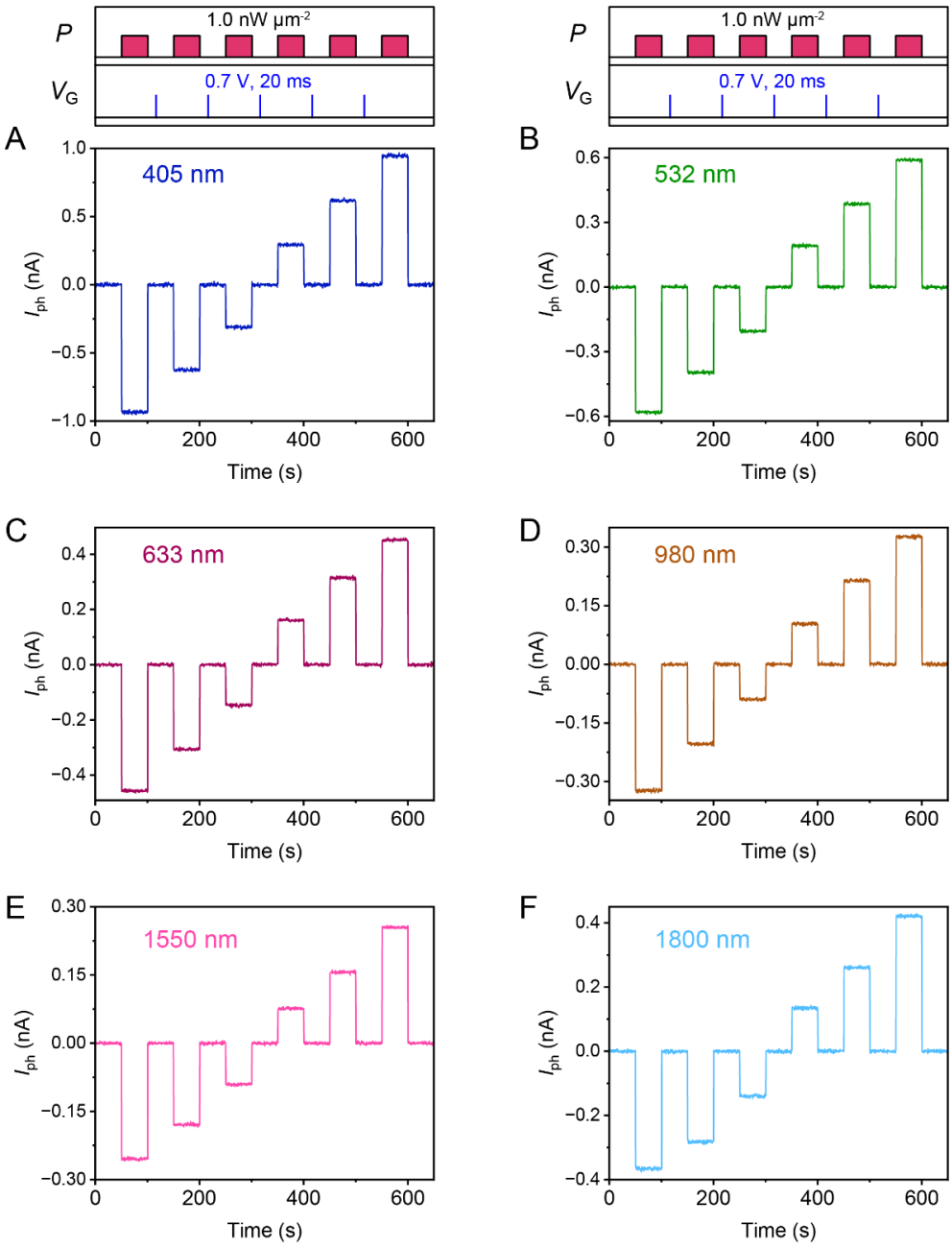

Fig. S26 Photoresponse of the device triggered by optical pulses with wavelengths of 405 nm (**A**), 532 nm (**B**), 633 nm (**C**), 980 nm (**D**), 1550 nm (**E**), and 1800 nm (**F**), respectively. Positive V_G pulses (0.7 V, 20 ms) were applied to the device to modulate the responsivity, and the photocurrents were measured by irradiating light pulses (1.0 nW μm^{-2}) with corresponding wavelengths. Here the duration of each optical pulse is 50 s, and such a long duration is used to demonstrate that the photocurrents do not change with prolonging the illumination time, which is crucial for the computing accuracy of the neural network.

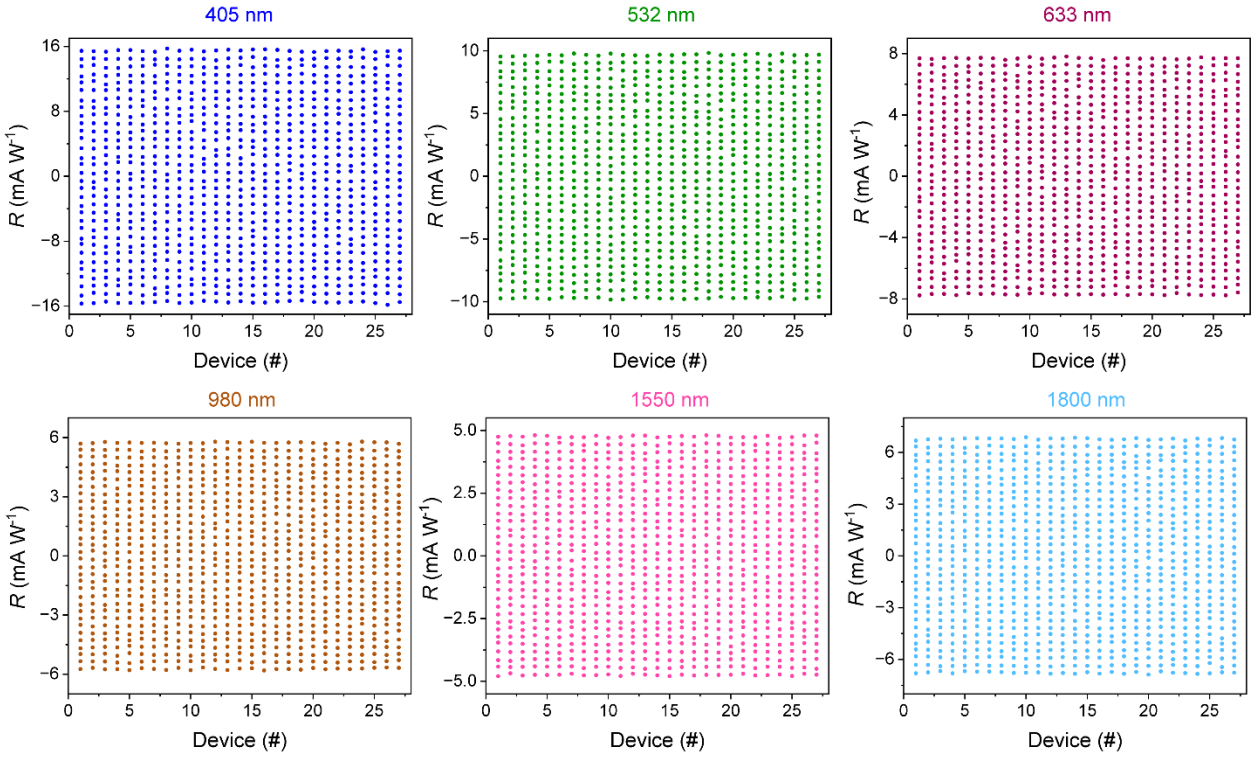

Fig. S27 32 responsivity states achieved by the 27 devices for wavelengths of 405 nm (blue), 532 nm (green), 633 nm (dark red), 980 nm (brown), 1550 nm (pink), and 1800 nm (cyan), respectively, using the closed-loop programming method.

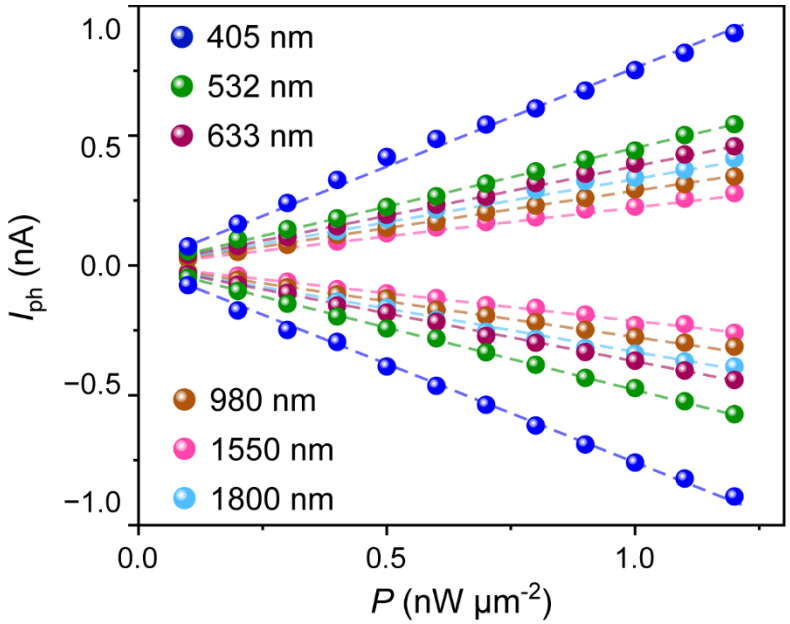

Fig. S28 The linearly light-intensity-dependent photoresponse of the vision sensor for different wavelengths.

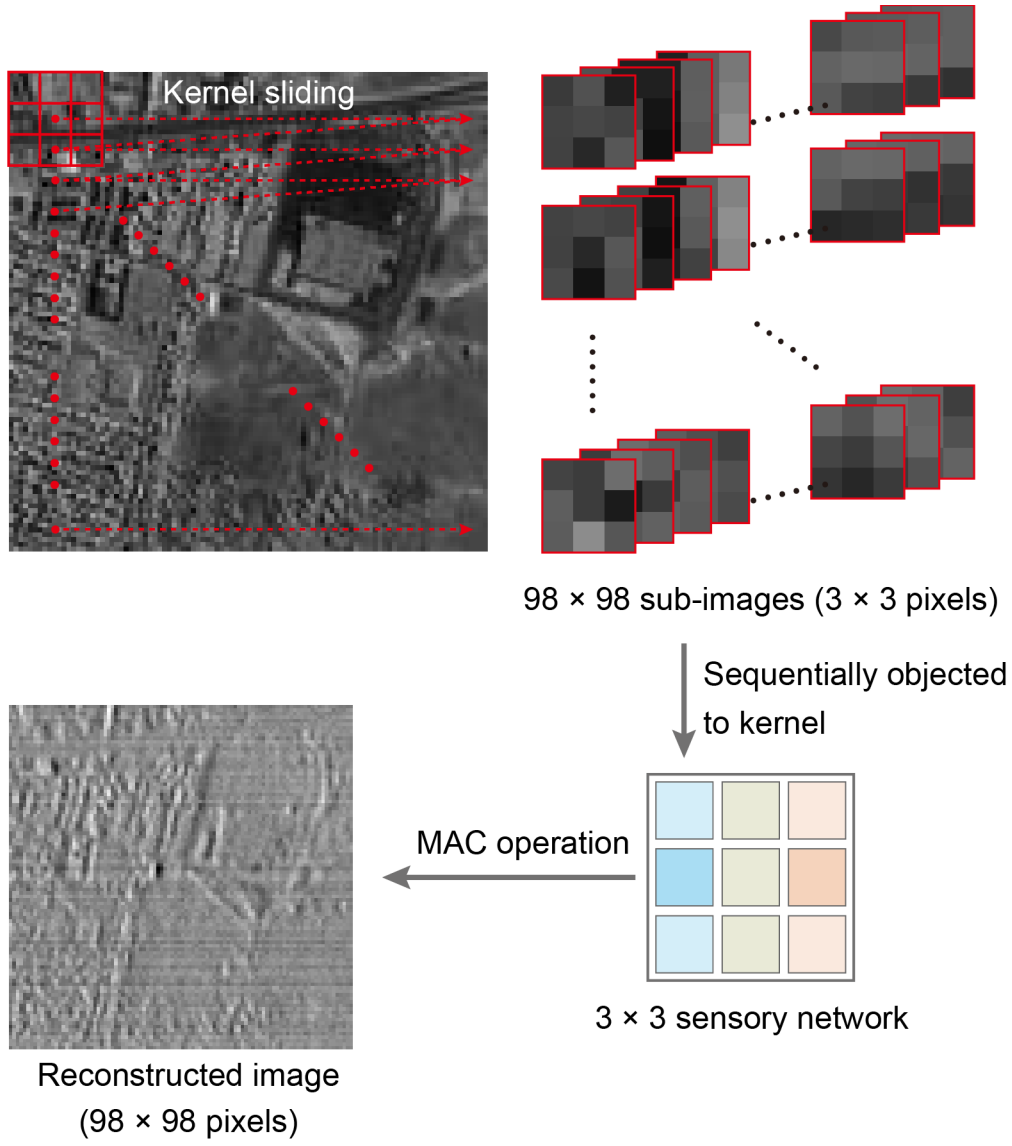

Fig. S29 Illustration of convolutional processing for hyperspectral images. Original image (100 × 100 pixels) was first divided into 98 × 98 sub-images with 3 × 3 pixels, mimicking the sliding of a 3 × 3 kernel with a step of 1. These sub-images were sequentially objected into the 3 × 3 sensor array with pre-defined responsivity distribution to implement in-sensor MAC operations. By measuring the total photocurrents generated by the sensory network, each sub-image was converted to a photocurrent value, which was used to reconstruct a 98 × 98-pixel image as the processed image.

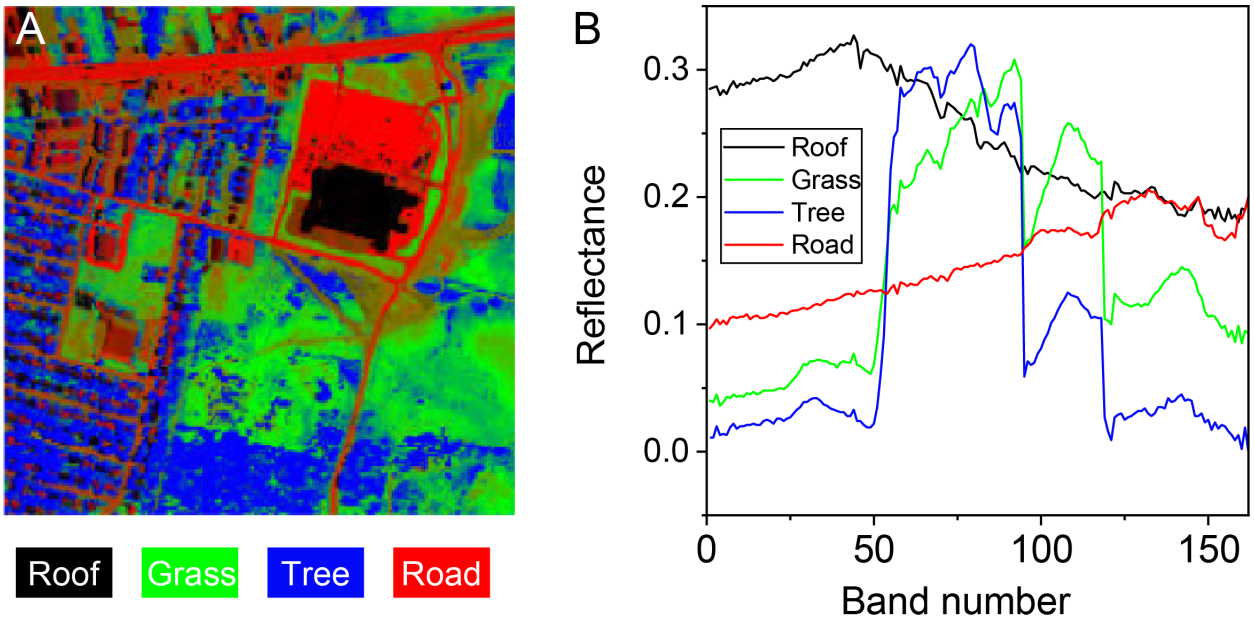

Fig. S30 Hyperspectral images of Urban. Spatial (**A**) and spectral (**B**) distribution of the four endmembers, roof, grass, tree, and road, in the hyperspectral images of Urban (https://rslab.ut.ac.ir/data) (*40*).

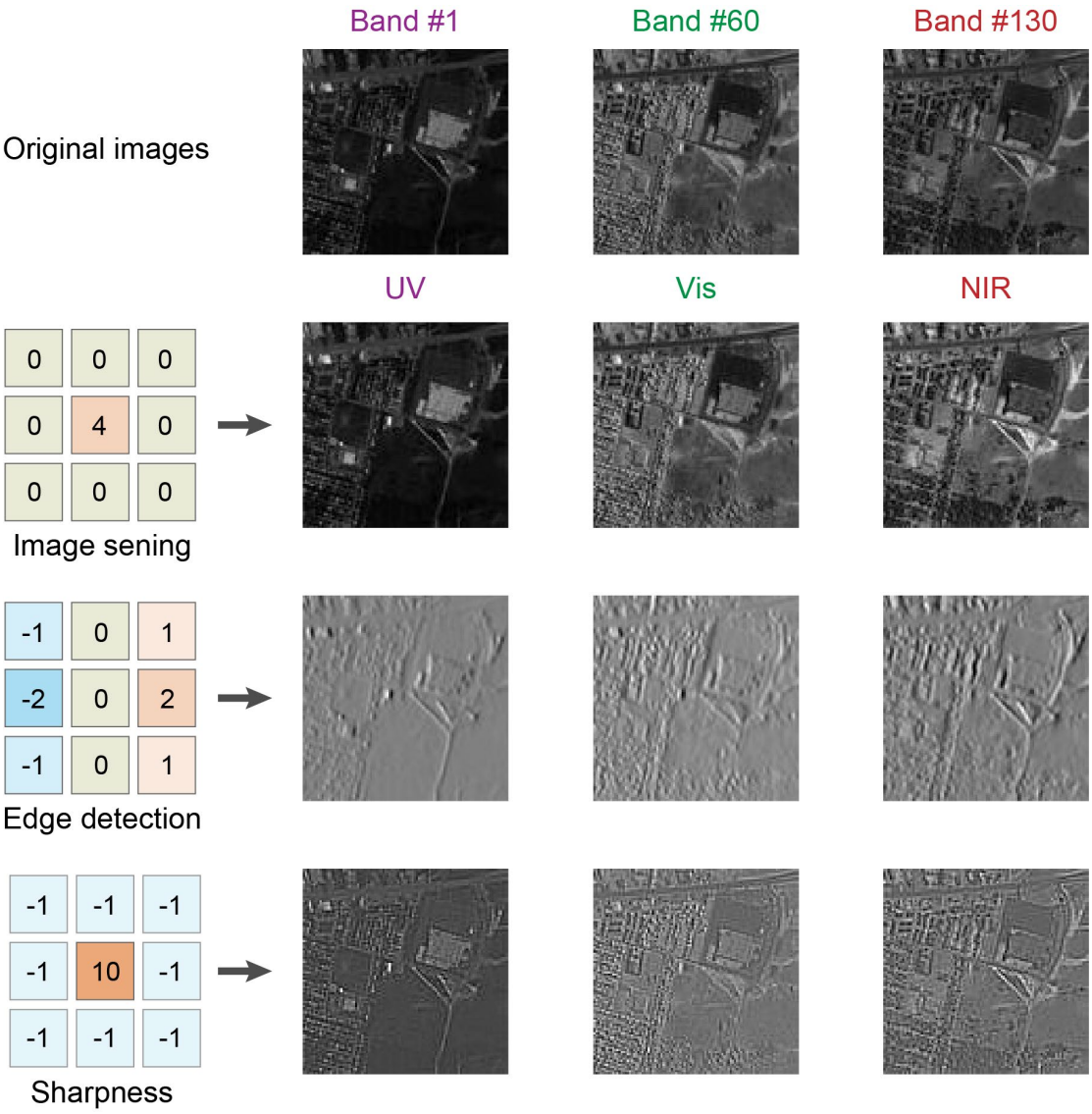

Fig. S31 Simulation results of the convolutional processing for hyperspectral images in UV, vis, and NIR regime. Different weight distributions were defined to realize functions of image sensing, edge detection, and sharpness.

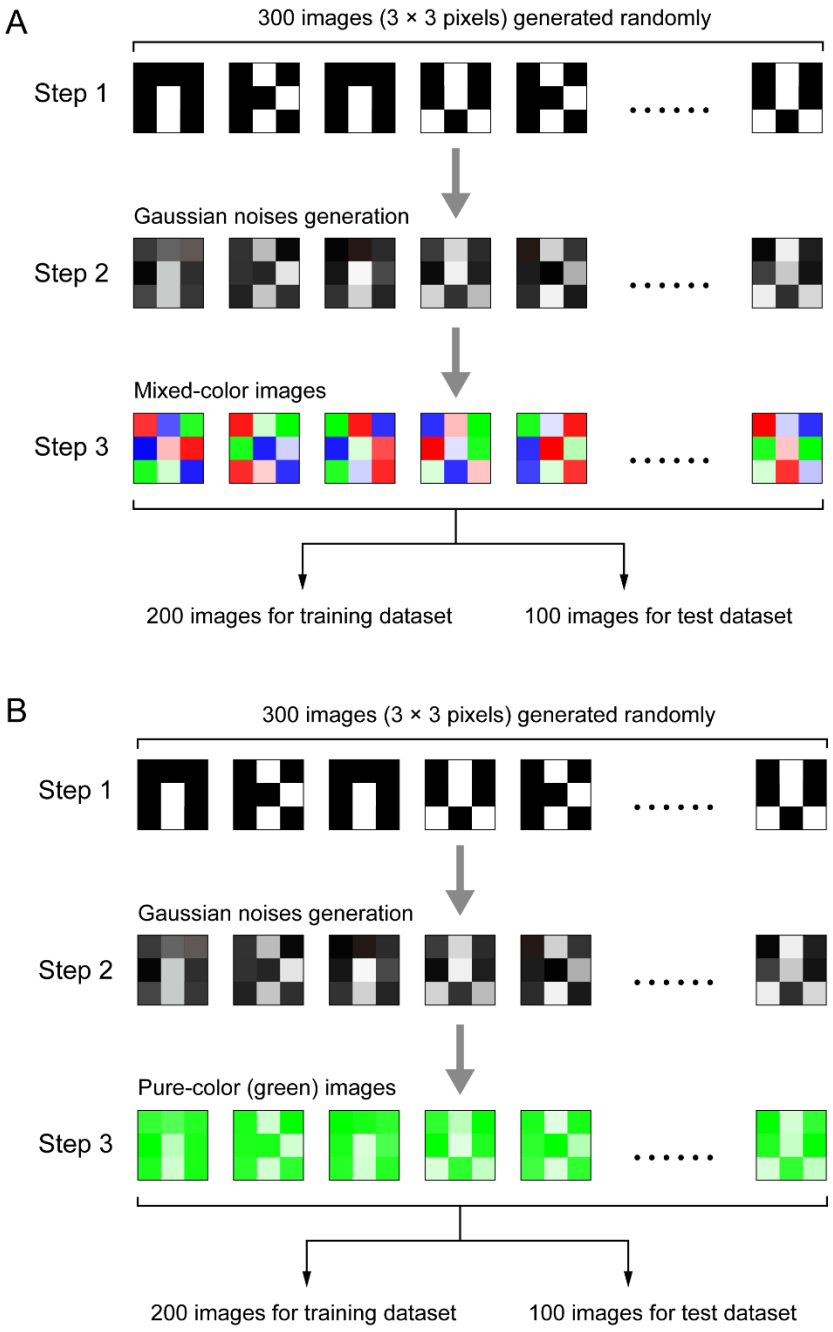

Fig. S32 Generation of the training and test datasets. (**A**) Processes for the generation of mixed-color images with Gaussian noises. Step 1, 300 images (3 × 3 pixels) with letters of "n", "k", and "u" are randomly generated, with intensities of "255" and "0" for the occupied and blank pixels, respectively. Step 2, the pixel values of the generated training and test images are normalized to 0–1, followed by adding the randomly generated Gaussian noises (σ = 0, 0.1, 0.2, and 0.3, respectively), and then the pixel values of each image are normalized to 0–255 again. Step 3, the 9 pixels in each image are randomly divided into 3 groups, and each group corresponds one color

(blue, green, and red). These 300 images are randomly divided two groups: 200 images as training dataset and 100 images as test dataset. (**B**) Processes for the generation of pure-color images with Gaussian noises. The first two steps are the same with that of the mixed-color images, while the last step only one color (for example, green) instead of three colors is added to these images. In these images, the pixel values corresponded to the intensities of the input light, with corresponding wavelengths. In the autoencoding experiment, the gray-scale images were projected to the sensor arrays using a 532 nm laser array, and thus the gray-scale image datasets can be considered as pure-color (green) images.

Fig. S33 Training and test datasets with noise level of σ = 0.2 for color image classification task.

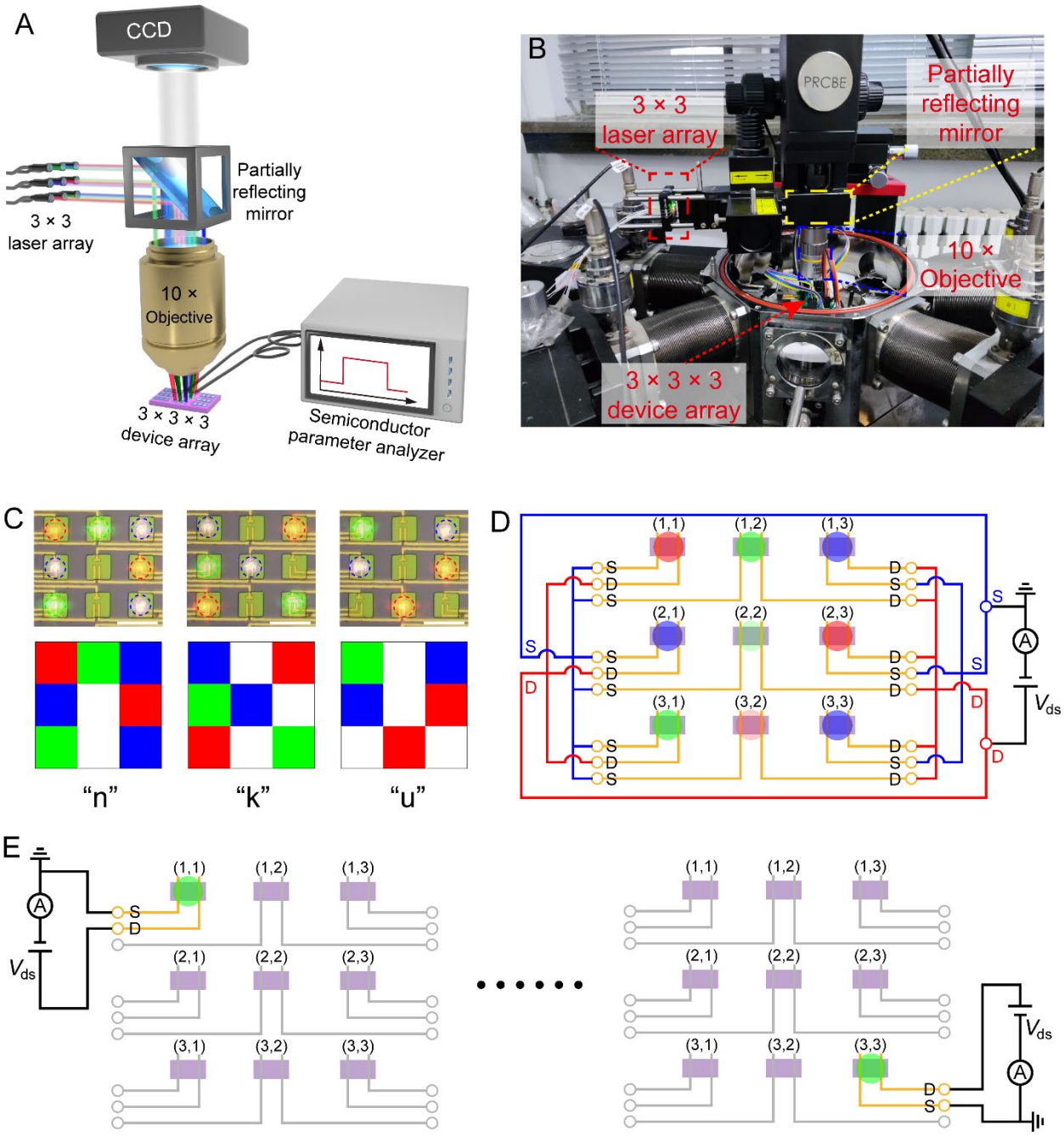

Fig. S34 Measurement system for the sensor array. (**A**,**B**) Schematic and photograph of the equipment for the projection of 3 × 3-pixel images to the sensor array. A 3 × 3 fiber laser array is equipped on a probe station. The 3 × 3 light signals emitted by the lasers with corresponding wavelengths enter the microscope and are focused by a 10× objective lens. The focused light spots are projected on the 3 × 3 device array, and the total photocurrents are measured by the Keithley 4200A-SCS. (**C**) Optical images of the projected images of "n", "k" and "u" on the 3 × 3 sensor array. Scale bars. 50 μm. The size of the focused light spots is approximately 20 μm, which are

marked with corresponding colors. (**D**) Schematic of the circuit for the measurement of the total photocurrent generated by the 3 × 3 sensor array while projecting 3 × 3-pixel images. The 3 × 3 purple rectangles represent the sensor array, while the blue/green/red circles represent the light spots illuminated on the devices. The nine sensors are connected in parallel and the photocurrents generated by the nine sensors are summed via Kirchhoff's law. V_{ds} = 0.1 V. (**E**) Schematic for the measurement of the responsivities of the 3 × 3 sensor array. The equipment is similar to (**B**), but only one 532 nm (1.0 nW cm^{-2}) light is focused on one device each time. The responsivity is measured from the first device ((1,1), left panel) using Keithley 4200A-SCS, and then switch to the second, the third, …, the 9^{th} device ((3,3), right panel) in sequence. The responsivities of the sensor array are measured one device by one device. V_{ds} = 0.1 V.

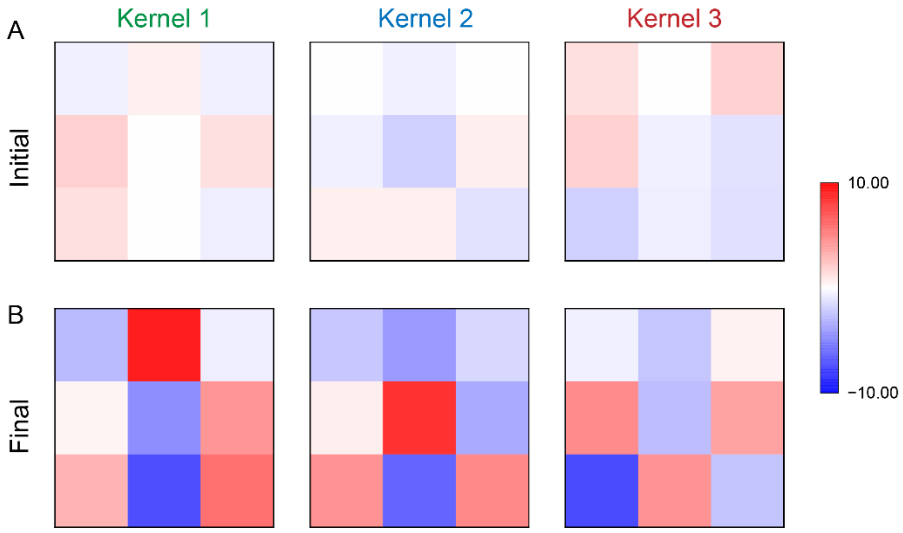

Fig. S35 Responsivity distributions of the three kernels in the classifier before (**A**) and after (**B**) training.

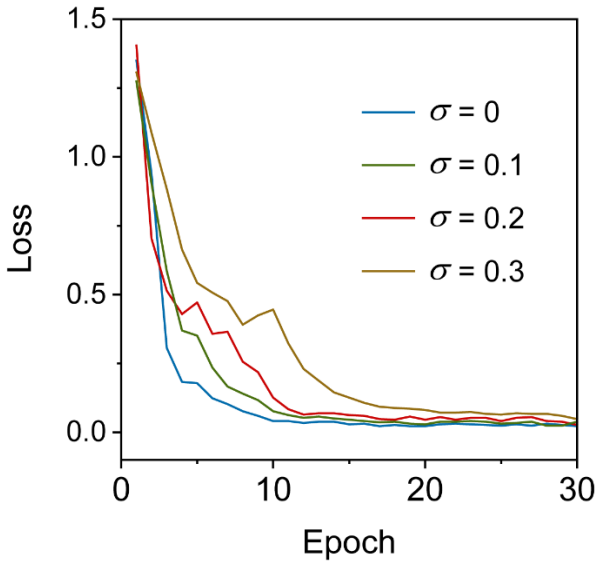

Fig. S36 Loss of the classifier for different noise levels during the training.

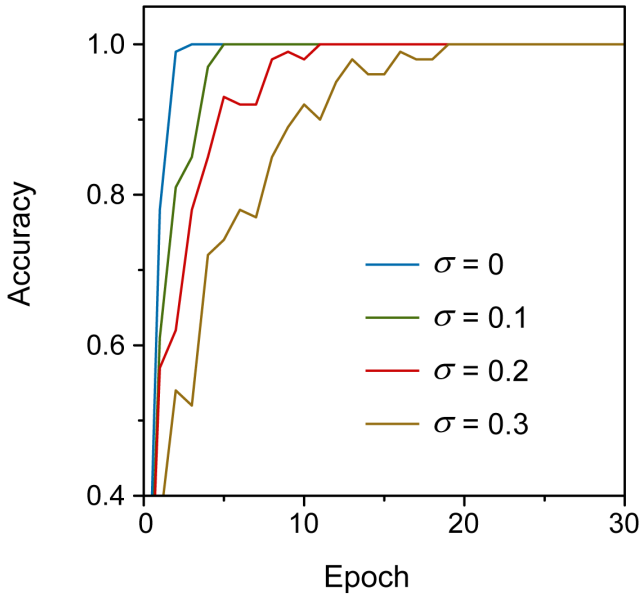

Fig. S37 Classification accuracy of the classifier for pure-color images with different noise levels. Since the device illuminated by different wavelengths would generate different photocurrents, i.e., wavelength-dependent photoresponse, the total generated photocurrent in each kernel varies while the color of the input images changes, which would degrade the recognition efficiency and accuracy of the classifier for mixed-color images. To evaluate the influence of the wavelength-dependent photoresponse of the vision sensors on the classification accuracy for mixed-color images, here the classification tasks for pure-color images were implemented. The training and text datasets with pure-color images with different noise levels were randomly generated following the steps as described in fig. S32B. Compared with the classification of mixed-color images (Fig. 5D in the main text), less epochs were required to reach a 100% recognition accuracy for each noise level. Thus the wavelength-dependent photoresponse would induce a slightly degradation in recognition efficiency for mixed-color images.

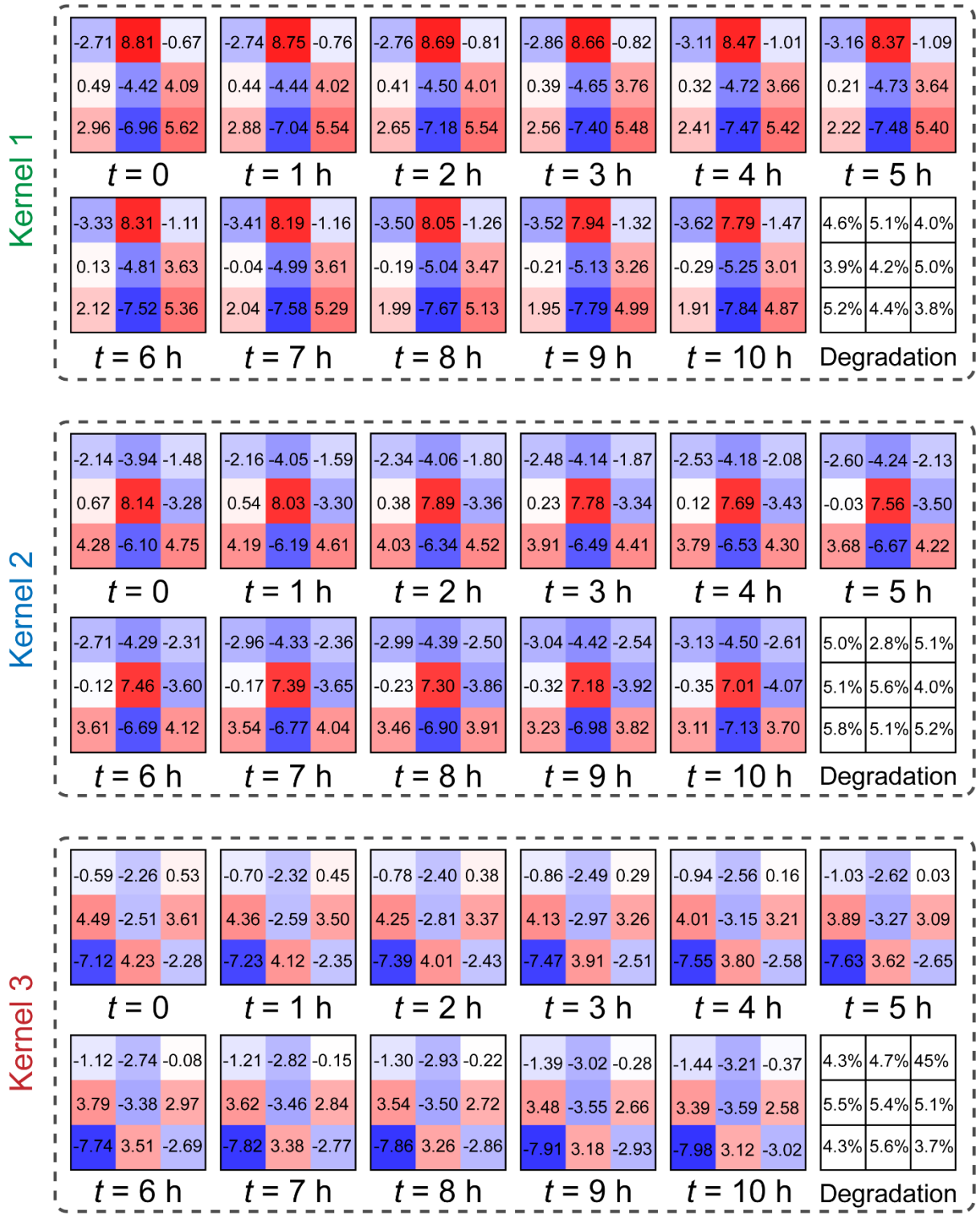

Fig. S38 Evolution of the responsivity distributions of the three kernels in the classifier after training with different latency. The last panel in each box describes the degradation of the responsivity in 10 h, which are calculated by $\Delta R/20 \times 100\%$, where ΔR is the change of responsivity in 10 h, and factor 20 is the whole range of the responsivity (–10 to 10 mA W^{-1}).

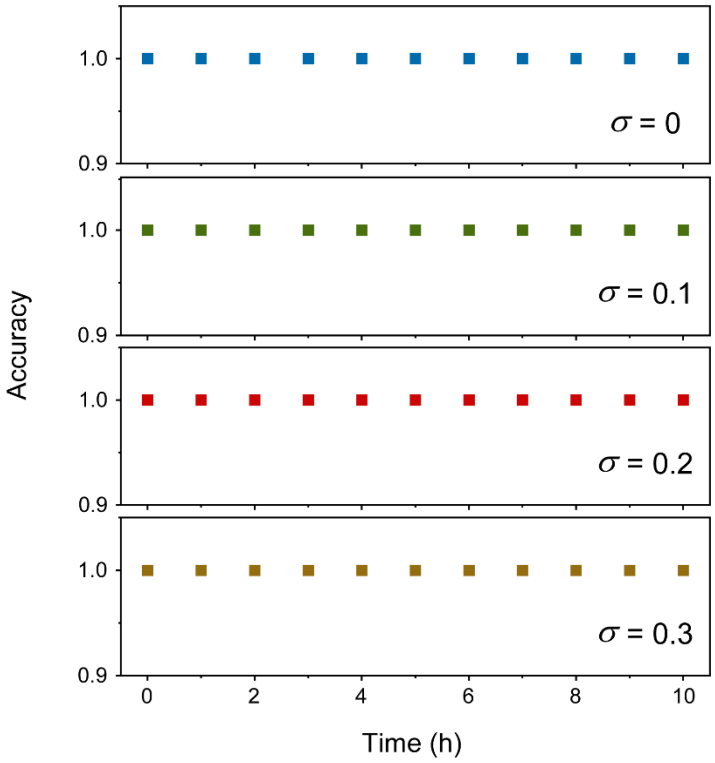

Fig. S39 Classification accuracy of the classifier after training as a function of weight storage time. For each noise level (σ = 0, 0.1, 0.2, and 0.3), the classifier was trained for 30 epochs to reach a 100% recognition accuracy for the color images with corresponding noise level. Then, the test dataset with corresponding noise level was input to the trained classifier every 1 h, and the classifier maintained a 100% recognition accuracy for the test dataset even after 10 h.

Fig. S40 Training and test datasets with noise level of σ = 0.2 for grayscale image autoencoding task.

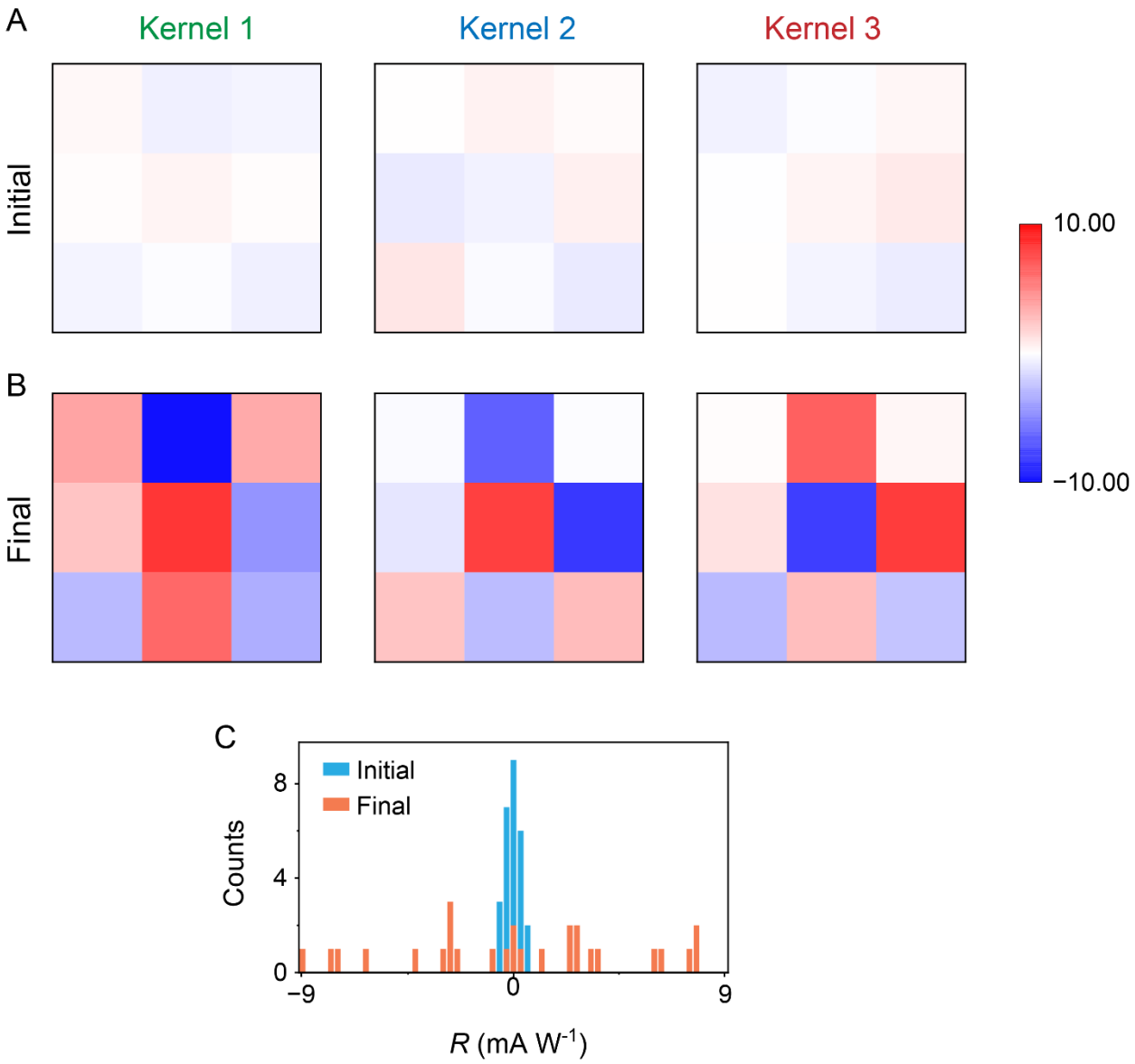

Fig. S41 Responsivity distributions of the three kernels in the encoder before (**A**) and after (**B**) training. (**C**) Histogram of the initial and final responsivity values of the three kernels.

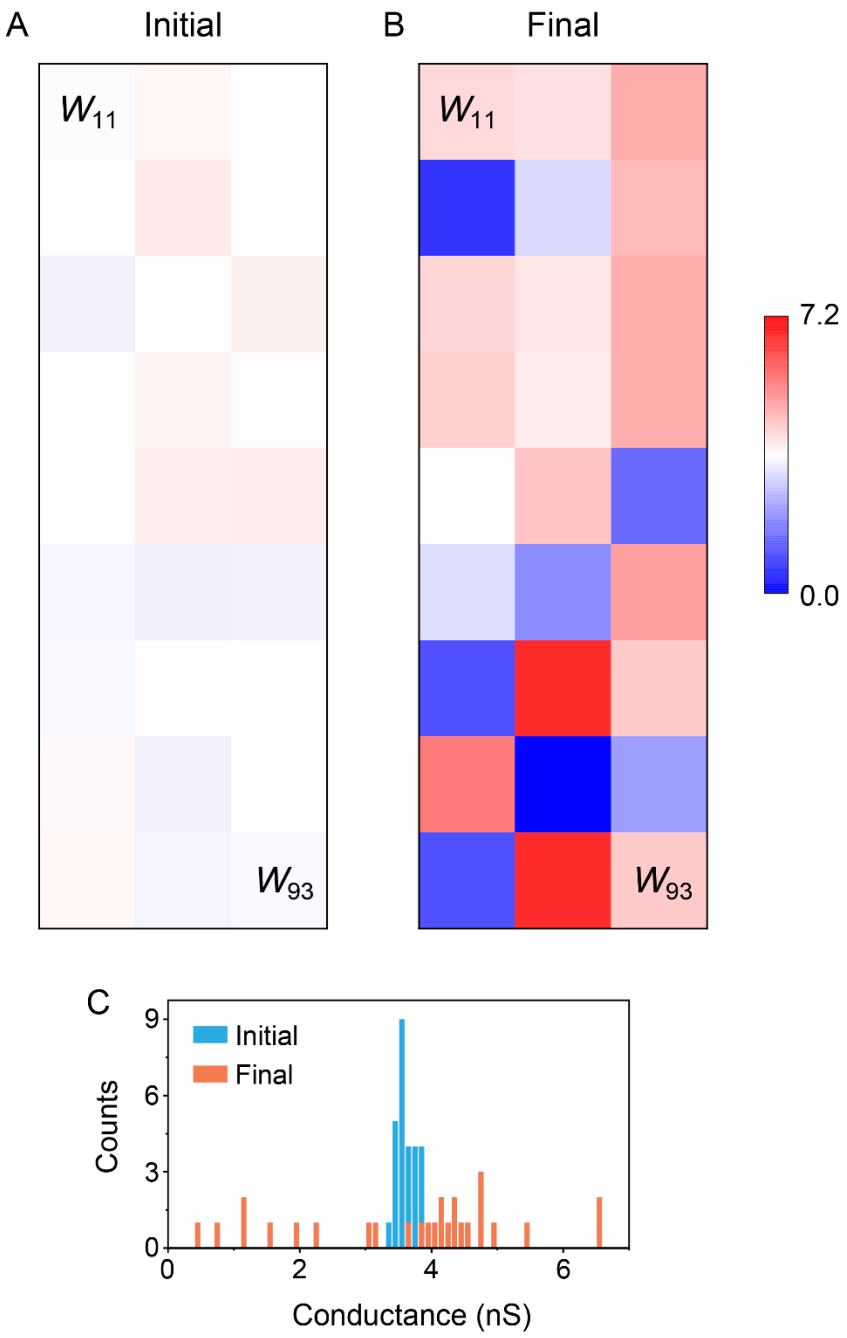

Fig. S42 Conductance distributions of the 9 × 3 device array in the decoder before (**A**) and after (**B**) training. (**C**) Histogram of the initial and final conductance values of the decoder.

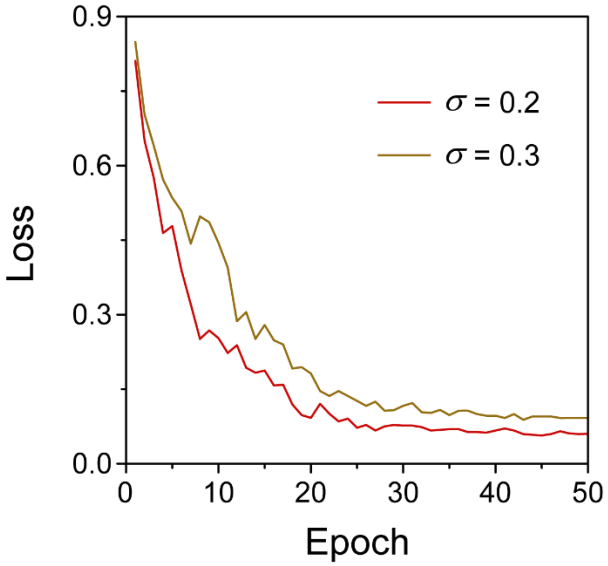

Fig. S43 Loss of the autoencoder for noise levels of σ = 0.2 and 0.3 during the training.

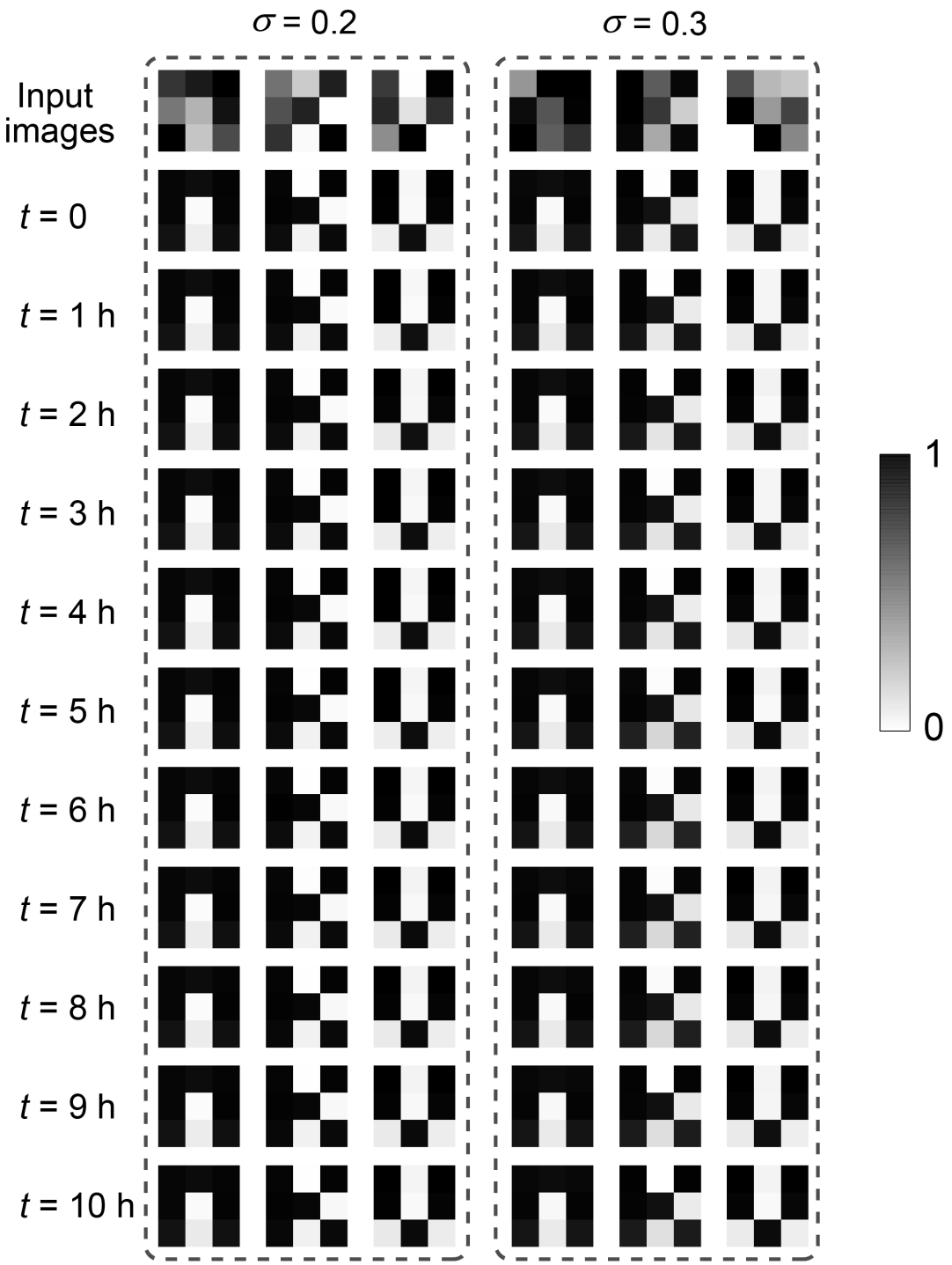

Fig. S44 Evolution of the reconstructed images performed by the autoencoder after training with different latency. The weights were locally stored in the network, and autoencoding tasks for grayscale images with noise levels of σ = 0.2 and 0.3 were performed every 1 hour. The degradation of the weights is within 5% in 10 h, and thus the reconstructed images with reduced noises and enhanced contrast do not have obvious change.

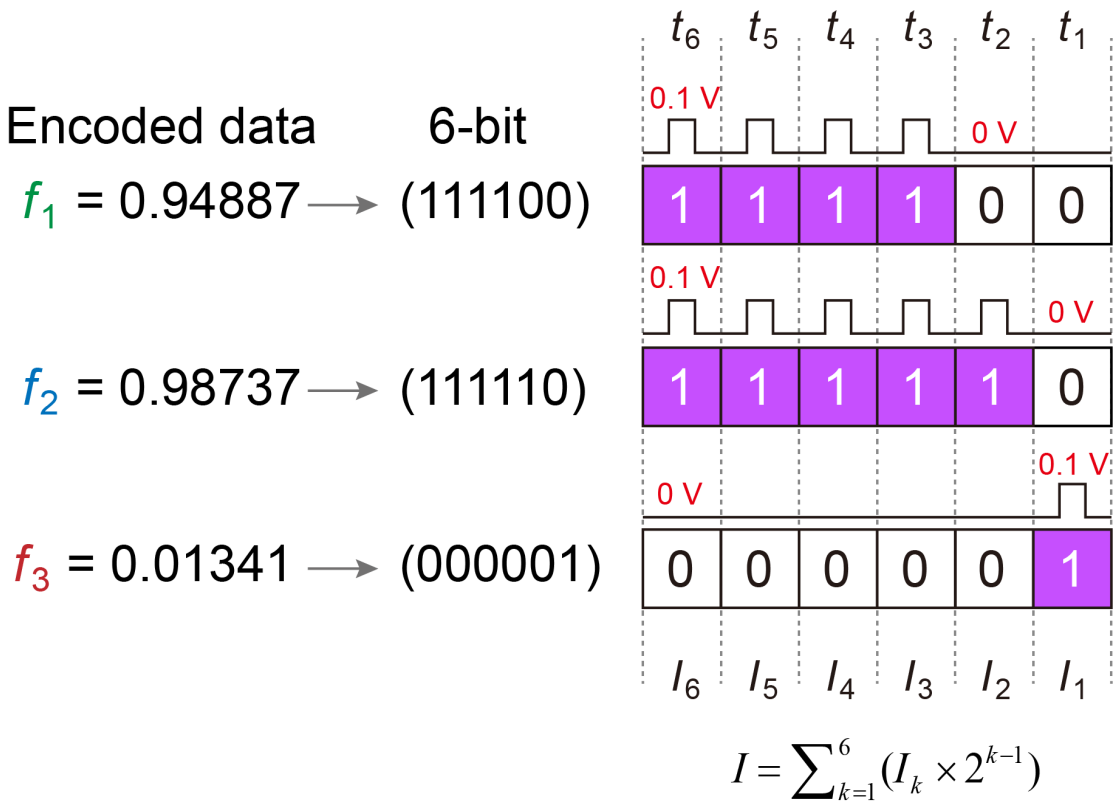

Fig. S45 Conversion of encoded data to 6-bit precision binary voltage inputs. In the autoencoder, the encoded data, f_1, f_2, and f_3, were quantized to binary values with 6-bit precision. The input voltage signals to the decoder were divided into six intervals (t_1, t_2, …, t_6), and each '1' at a certain bit location implied a 0.1 V read voltage pulse, while a '0' indicates a 0 V read voltage pulse. The corresponding output current I_k (k = 1, 2, …, 6) at each time interval t_k was measured, and the total output current was summed by $I = \sum_{k=1}^{6} (I_k \times 2^{k-1})$ (*25*). Here sequential voltage pulses (with small amplitude of 0.1 V) were used to input the encoded data to the decoder since such a small voltage was safe for the device. It would not change the conductance state of the device while applying a 0.1 V voltage to the drain electrode.

Table S1. Parameters of the retinomorphic vision sensors for in-sensor computing.

Device structure	Responsivity modulation				Spectral range	Self-power	Response speed	Array scale	Ref.
	Manner	Regime	Non-volatile	Linear					
Ambipolar WSe_2	Dual-gate bias	Positive/ Negative	N	Y	vis	Y	40 ns	3×3×3	(*1*)
WSe_2/hBN/ Al_2O_3	Gate bias	Positive/ Negative	N	Y	405-650 nm	N	8 ms	3×3×3	(*13*)
BP/Al_2O_3/ HfO_2/Al_2O_3	Floating gate	Positive	Y	--	MIR	N	--	4×3	(*17*)
$MoTe_2$/ $PdSe_2$	Gate bias	Positive/ Negative	N	Y	365-980 nm	Y	0.4-4 μs	1[e)]	(*14*)
GaN/AlGaN/ HfO_2/OIHP[a)]	Gate bias	Positive/ Negative	N	--	457-660 nm	N	--	3×3	(*20*)
PZT/SRO/ STO[b)]	Ferroelectric polarization	Positive/ Negative	Y	Y	UV	Y	--	3×3	(*15*)
Gr/$MoS_{2-x}O_x$/ Gr[c)]	Redox of Gr electrodes	Positive[d)]	Y	Y	Sun light	N	--	3×3	(*16*)
SWNT@ GDY	Li^+ ions	Positive/ Negative	Y	Y	400-1800 nm	N	5 ms	3×3×3	This work

"N": No; "Y": Yes; "--": Not available.

[a)]OIHP: Organic–inorganic halide perovskite. [b)]PZT: $Pb(Zr_{0.2}Ti_{0.8})O_3$; SRO: $SrRuO_3$; STO: $SrTiO_3$. [c)]Gr: Graphene. [d)]Individual device can only realize positive response, and negative response was realized by parallel connection of two devices with opposite polarity. [e)]Parameters extracted from one device, and extended to a 3 × 3 array by simulation.

REFERENCES

1. L. Mennel, J. Symonowicz, S. Wachter, D. K. Polyushkin, A. J. Molina-Mendoza, T. Mueller, Ultrafast machine vision with 2D material neural network image sensors. *Nature* **579**, 62–66 (2020).

2. Y. Chai, In-sensor computing for machine vision. *Nature* **579**, 32–33 (2020).

3. D. Lee, M. Park, Y. Baek, B. Bae, J. Heo, K. Lee, In-sensor image memorization and encoding via optical neurons for bio-stimulus domain reduction toward visual cognitive processing. *Nat. Commun.* **13**, 5223 (2022).

4. F. Zhou, Y. Chai, Near-sensor and in-sensor computing. *Nat. Electron.* **3**, 664–671 (2020).

5. T. Wan, B. Shao, S. Ma, Y. Zhou, Q. Li, Y. Chai, In-sensor computing: Materials, devices, and integration technologies. *Adv. Mater.*, 2203830 (2022).

6. K. Liu, T. Zhang, B. Dang, L. Bao, L. Xu, C. Cheng, Z. Yang, R. Huang, Y. Yang, An optoelectronic synapse based on α-In_2Se_3 with controllable temporal dynamics for multimode and multiscale reservoir computing. *Nat. Electron.* **5**, 761–773 (2022).

7. Z. Zhang, X. Zhao, X. Zhang, X. Hou, X. Ma, S. Tang, Y. Zhang, G. Xu, Q. Liu, S. Long, In-sensor reservoir computing system for latent fingerprint recognition with deep ultraviolet photo-synapses and memristor array. *Nat. Commun.* **13**, 6590 (2022).

8. L. Sun, Z. Wang, J. Jiang, Y. Kim, B. Joo, S. Zheng, S. Lee, W. J. Yu, B.-S. Kong, H. Yang, In-sensor reservoir computing for language learning via two-dimensional memristors. *Sci. Adv.* **7**, eabg1455 (2021).

9. F. Zhou, Z. Zhou, J. Chen, T. H. Choy, J. Wang, N. Zhang, Z. Lin, S. Yu, J. Kang, H. S. P. Wong, Y. Chai, Optoelectronic resistive random access memory for neuromorphic vision sensors. *Nat. Nanotechnol.* **14**, 776–782 (2019).

10. Y.-X. Hou, Y. Li, Z.-C. Zhang, J.-Q. Li, D.-H. Qi, X.-D. Chen, J.-J. Wang, B.-W. Yao, M.-X. Yu, T.-B. Lu, Large-scale and flexible optical synapses for neuromorphic computing and integrated visible information sensing memory processing. *ACS Nano* **15**, 1497–1508 (2021).

11. Z.-C. Zhang, Y. Li, J.-J. Wang, D.-H. Qi, B.-W. Yao, M.-X. Yu, X.-D. Chen, T.-B. Lu, Synthesis of wafer-scale graphdiyne/graphene heterostructure for scalable neuromorphic computing and artificial visual systems. *Nano Res.* **14**, 4591–4600 (2021).

12. B. Dang, K. Liu, X. Wu, Z. Yang, L. Xu, Y. Yang, R. Huang, One-phototransistor–one-memristor array with high-linearity light-tunable weight for optic neuromorphic computing. *Adv. Mater.*, 2204844 (2022).

13. C.-Y. Wang, S.-J. Liang, S. Wang, P. Wang, Z. Li, Z. Wang, A. Gao, C. Pan, C. Liu, J. Liu, H. Yang, X. Liu, W. Song, C. Wang, X. Wang, K. Chen, Z. Wang, K. Watanabe, T. Taniguchi, J. J. Yang, F. Miao, Gate-tunable van der Waals heterostructure for reconfigurable neural network vision sensor. *Sci. Adv.* **6**, eaba6173 (2020).

14. L. Pi, P. Wang, S.-J. Liang, P. Luo, H. Wang, D. Li, Z. Li, P. Chen, X. Zhou, F. Miao, T. Zhai, Broadband convolutional processing using band-alignment-tunable heterostructures. *Nat. Electron.* **5**, 248–254 (2022).

15. B. Cui, Z. Fan, W. Li, Y. Chen, S. Dong, Z. Tan, S. Cheng, B. Tian, R. Tao, G. Tian, D. Chen, Z. Hou, M. Qin, M. Zeng, X. Lu, G. Zhou, X. Gao, J.-M. Liu, Ferroelectric photosensor network: An advanced hardware solution to real-time machine vision. *Nat. Commun.* **13**, 1707 (2022).

16. X. Fu, T. Li, B. Cai, J. Miao, G. N. Panin, X. Ma, J. Wang, X. Jiang, Q. Li, Y. Dong, C. Hao, J. Sun, H. Xu, Q. Zhao, M. Xia, B. Song, F. Chen, X. Chen, W. Lu, W. Hu, Graphene/$MoS_{2-x}O_x$/graphene photomemristor with tunable non-volatile responsivities for neuromorphic vision processing. *Light-Sci. Appl.* **12**, 39 (2023).

17. S. Lee, R. Peng, C. Wu, M. Li, Programmable black phosphorus image sensor for broadband optoelectronic edge computing. *Nat. Commun.* **13**, 1485 (2022).

18. Y. Wang, Y. Cai, F. Wang, J. Yang, T. Yan, S. Li, Z. Wu, X. Zhan, K. Xu, J. He, Z. Wang, A three-dimensional neuromorphic photosensor array for nonvolatile in-sensor computing. *Nano Lett.* **23**, 4524–4532 (2023).

19. S. Wang, C.-Y. Wang, P. Wang, C. Wang, Z.-A. Li, C. Pan, Y. Dai, A. Gao, C. Liu, J. Liu, H. Yang, X. Liu, B. Cheng, K. Chen, Z. Wang, K. Watanabe, T. Taniguchi, S.-J. Liang, F. Miao, Networking retinomorphic sensor with memristive crossbar for brain-inspired visual perception. *Natl. Sci. Rev.* **8**, nwaa172 (2021).

20. X. Hong, Y. Huang, Q. Tian, S. Zhang, C. Liu, L. Wang, K. Zhang, J. Sun, L. Liao, X. Zou, Two-dimensional perovskite-gated AlGaN/GaN high-electron-mobility-transistor for neuromorphic vision sensor. *Adv. Sci.* **9**, 2202019 (2022).

21. F. Liao, Z. Zhou, B. J. Kim, J. Chen, J. Wang, T. Wan, Y. Zhou, A. T. Hoang, C. Wang, J. Kang, J.-H. Ahn, Y. Chai, Bioinspired in-sensor visual adaptation for accurate perception. *Nat. Electron.* **5**, 84–91 (2022).

22. T. Euler, S. Haverkamp, T. Schubert, T. Baden, Retinal bipolar cells: Elementary building blocks of vision. *Nat. Rev. Neurosci.* **15**, 507–519 (2014).

23. C. Li, M. Hu, Y. Li, H. Jiang, N. Ge, E. Montgomery, J. Zhang, W. Song, N. Dávila, C. E. Graves, Z. Li, J. P. Strachan, P. Lin, Z. Wang, M. Barnell, Q. Wu, R. S. Williams, J. J. Yang, Q. Xia, Analogue signal and image processing with large memristor crossbars. *Nat. Electron.* **1**, 52–59 (2018).

24. D. Ielmini, H.-S. P. Wong, In-memory computing with resistive switching devices. *Nat. Electron.* **1**, 333–343 (2018).

25. P. Yao, H. Wu, B. Gao, J. Tang, Q. Zhang, W. Zhang, J. J. Yang, H. Qian, Fully hardware-implemented memristor convolutional neural network. *Nature* **577**, 641–646 (2020).

26. A. Sebastian, M. Le Gallo, R. Khaddam-Aljameh, E. Eleftheriou, Memory devices and applications for in-memory computing. *Nat. Nanotechnol.* **15**, 529–544 (2020).

27. X.-H. Wang, Z.-C. Zhang, J.-J. Wang, X.-D. Chen, B.-W. Yao, Y.-X. Hou, M.-X. Yu, Y. Li, T.-B. Lu, Synthesis of wafer-scale monolayer pyrenyl graphdiyne on ultrathin hexagonal boron nitride for multibit optoelectronic memory. *ACS Appl. Mater. Interfaces* **12**, 33069–33075 (2020).

28. Z. C. Zhang, Y. Li, J. Li, X. D. Chen, B. W. Yao, M. X. Yu, T. B. Lu, J. Zhang, An ultrafast nonvolatile memory with low operation voltage for high-speed and low-power applications. *Adv. Funct. Mater.* **31**, 2102571 (2021).

29. F.-D. Wang, M.-X. Yu, X.-D. Chen, J. Li, Z.-C. Zhang, Y. Li, G.-X. Zhang, K. Shi, L. Shi, M. Zhang, T.-B. Lu, J. Zhang, Optically modulated dual-mode memristor arrays based on core-shell $CsPbBr_3$@graphdiyne nanocrystals for fully memristive neuromorphic computing hardware. *SmartMat* **4**, e1135 (2023).

30. X. Gao, Y. Zhu, D. Yi, J. Zhou, S. Zhang, C. Yin, F. Ding, S. Zhang, X. Yi, J. Wang, Ultrathin graphdiyne film on graphene through solution-phase van der Waals epitaxy. *Sci. Adv.* **4**, eaat6378 (2018).

31. Y. Li, Z. C. Zhang, J. Li, X.-D. Chen, Y. Kong, F.-D. Wang, G.-X. Zhang, T.-B. Lu, J. Zhang, Low-voltage ultrafast nonvolatile memory via direct charge injection through a threshold resistive-switching layer. *Nat. Commun.* **13**, 4591 (2022).

32. B. W. Yao, J. Li, X. D. Chen, M. X. Yu, Z. C. Zhang, Y. Li, T. B. Lu, J. Zhang, Non-volatile electrolyte-gated transistors based on graphdiyne/MoS_2 with robust stability for low-power neuromorphic computing and logic-in-memory. *Adv. Funct. Mater.* **31**, 2100069 (2021).

33. Z.-C. Zhang, X.-D. Chen, T.-B. Lu, Recent progress in neuromorphic and memory devices based on graphdiyne. *Sci. Technol. Adv. Mat.* **24**, 2196240 (2023).

34. E. J. Fuller, S. T. Keene, A. Melianas, Z. Wang, S. Agarwal, Y. Li, Y. Tuchman, C. D. James, M. J. Marinella, J. J. Yang, A. Salleo, A. A. Talin, Parallel programming of an ionic floating-gate memory array for scalable neuromorphic computing. *Science* **364**, 570–574 (2019).

35. Y. van de Burgt, E. Lubberman, E. J. Fuller, S. T. Keene, G. C. Faria, S. Agarwal, M. J. Marinella, A. Alec Talin, A. Salleo, A non-volatile organic electrochemical device as a low-voltage artificial synapse for neuromorphic computing. *Nat. Mater.* **16**, 414–418 (2017).

36. J. Wen, W. Tang, Z. Kang, Q. Liao, M. Hong, J. Du, X. Zhang, H. Yu, H. Si, Z. Zhang, Y. Zhang, Direct charge trapping multilevel memory with graphdiyne/MoS_2 van der waals heterostructure. *Adv. Sci.* **8**, 2101417 (2021).

37. J. Li, Z. Zhang, Y. Kong, B. Yao, C. Yin, L. Tong, X. Chen, T. Lu, J. Zhang, Synthesis of wafer-scale ultrathin graphdiyne for flexible optoelectronic memory with over 256 storage levels. *Chem* **7**, 1284–1296 (2021).

38. B. R. Conway, Color vision, cones, and color-coding in the cortex. *Neuroscientist* **15**, 274–290 (2009).

39. Y. Li, J. Lu, D. Shang, Q. Liu, S. Wu, Z. Wu, X. Zhang, J. Yang, Z. Wang, H. Lv, M. Liu, Oxide-based electrolyte-gated transistors for spatiotemporal information processing. *Adv. Mater.* **32**, 2003018 (2020).

40. M. Gomroki, M. Hasanlou, P. Reinartz, STCD-EffV2T Unet: Semi transfer learning EfficientNetV2 T-Unet network for urban/land cover change detection using Sentinel-2 satellite images. *Remote Sens. (Basel)* **15**, 1232 (2023).

41. G. Li, Y. Li, H. Liu, Y. Guo, Y. Li, D. Zhu, Architecture of graphdiyne nanoscale films. *Chem. Commun.* **46**, 3256–3258 (2010).

42. J. Yao, Y. Li, Y. Li, Q. Sui, H. Wen, L. Cao, P. Cao, L. Kang, J. Tang, H. Jin, S. Qiu, Q. Li, Rapid annealing and cooling induced surface cleaning of semiconducting carbon nanotubes for high-performance thin-film transistors. *Carbon* **184**, 764–771 (2021).

43. Y. Liu, F. Wang, X. Wang, X. Wang, E. Flahaut, X. Liu, Y. Li, X. Wang, Y. Xu, Y. Shi, R. Zhang, Planar carbon nanotube-graphene hybrid films for high-performance broadband photodetectors. *Nat. Commun.* **6**, 8589 (2015).

44. S. Dai, Y. Zhao, Y. Wang, J. Zhang, L. Fang, S. Jin, Y. Shao, J. Huang, Recent advances in transistor-based artificial synapses. *Adv. Funct. Mater.* **29**, 1903700 (2019).

45. S. Jiang, S. Nie, Y. He, R. Liu, C. Chen, Q. Wan, Emerging synaptic devices: From two-terminal memristors to multiterminal neuromorphic transistors. *Mater. Today Nano* **8**, 100059 (2019).

46. J. Jiang, J. Guo, X. Wan, Y. Yang, H. Xie, D. Niu, J. Yang, J. He, Y. Gao, Q. Wan, 2D MoS_2 neuromorphic devices for brain-like computational systems. *Small* **13**, 1700933 (2017).

47. D. Liu, Q. Shi, S. Dai, J. Huang, The design of 3D-interface architecture in an ultralow-power, electrospun single-fiber synaptic transistor for neuromorphic computing. *Small* **16**, 1907472 (2020).

48. C. S. Yang, D. S. Shang, N. Liu, E. J. Fuller, S. Agrawal, A. A. Talin, Y. Q. Li, B. G. Shen, Y. Sun, All-solid-state synaptic transistor with ultralow conductance for neuromorphic computing. *Adv. Funct. Mater.* **28**, 1804170 (2018).

49. E. J. Fuller, F. E. Gabaly, F. Léonard, S. Agarwal, S. J. Plimpton, R. B. Jacobs-Gedrim, C. D. James, M. J. Marinella, A. A. Talin, Li-ion synaptic transistor for low power analog computing. *Adv. Mater.* **29**, 1604310 (2017).

50. J. Lee, L. G. Kaake, J. H. Cho, X. Y. Zhu, T. P. Lodge, C. D. Frisbie, Ion gel-gated polymer thin-film transistors: Operating mechanism and characterization of gate dielectric capacitance, switching speed, and stability. *J. Phys. Chem. C* **113**, 8972–8981 (2009).

51. C. Sun, D. J. Searles, Lithium storage on graphdiyne predicted by DFT calculations. *J. Phys. Chem. C* **116**, 26222–26226 (2012).

52. N. Wang, J. He, K. Wang, Y. Zhao, T. Jiu, C. Huang, Y. Li, Graphdiyne-based materials: Preparation and application for electrochemical energy storage. *Adv. Mater.* **31**, 1803202 (2019).

53. K. Kim, C.-L. Chen, T. Quyen, A. M. Shen, Y. Chen, A carbon nanotube synapse with dynamic logic and learning. *Adv. Mater.* **25**, 1693–1698 (2013).

54. S. Kazaoui, N. Minami, H. Kataura, Y. Achiba, Absorption spectroscopy of single-wall carbon nanotubes: Effects of chemical and electrochemical doping. *Synth. Met.* **121**, 1201–1202 (2001).